applied sciences

MDPI

Article

Optimization and Validation of a Micro-Centrifugal Pump Based on a CFD Simulation and Optimization Platform

Xuemin Wang *, Hao Wu and Yuxian Xia

Faculty of Intelligent Technology, Shanghai Institute of Technology, Shanghai 201418, China; haowu7405@gmail.com (H.W.); xiayuxian@sit.edu.cn (Y.X.)

* Correspondence: wangxuemin2008@163.com

Featured Application

The proposed integrated CFD simulation-optimization platform can be applied to the rapid design, optimization, and validation of micro-centrifugal pumps and other small-scale turbomachinery.

Abstract

Computational fluid dynamics (CFD) plays a crucial role in optimizing micro-centrifugal pump geometries; however, conventional workflows often suffer from fragmentation, manual intervention, and poor interoperability among software tools. In this study, an integrated CFD-based simulation–optimization platform was developed to establish a closed-loop workflow covering parametric modeling, automated meshing, steady CFD analysis, and multi-objective optimization. Using a micro-centrifugal pump as a case study, optimal Latin hypercube sampling, a Kriging surrogate model, and a multi-objective genetic algorithm were combined to quantify the relationships between key structural parameters and hydraulic performance and to identify Pareto-optimal designs. Sensitivity analysis showed that blade count and volute throat height were the dominant factors affecting pump head and efficiency. Compared with the baseline design, the optimized schemes achieved average improvements of 40.36% in head and 22.89% in hydraulic efficiency, with Scheme 1 showing the best overall balance. Experimental validation using hydraulic performance testing and particle image velocimetry showed that the deviation between predicted and measured heads was within 10%, and the measured flow-field trends agreed well with the CFD results. The proposed framework provides a reproducible method for the design optimization of micro-centrifugal pumps and other small-scale turbomachinery.

Keywords: CFD-based optimization platform; micro-centrifugal pump; multi-objective optimization; optimal Latin hypercube sampling; kriging surrogate; PIV validation

Check for updates

Academic Editor: Paolo Renna

Received: 7 April 2026
Revised: 28 April 2026
Accepted: 30 April 2026
Published: 7 May 2026

Copyright: © 2026 by the authors. Licensee MDPI, Basel, Switzerland. This article is an open access article distributed under the terms and conditions of the Creative Commons Attribution (CC BY) license.

1. Introduction

Micro-centrifugal pumps are widely employed in medical devices, electronic cooling, chemical processes, and small-scale energy systems owing to their compactness, operational stability, and broad flow-rate adaptability [1–3]. They also serve as core components in artificial heart pumps and extracorporeal circulation devices, where head generation, hydraulic efficiency, and flow stability directly affect the reliability of fluid transport [4]. Compared with conventional centrifugal pumps, micro-centrifugal pumps operate in narrow passages and at relatively low Reynolds numbers, where viscous effects, local losses, and geometric tolerances have a stronger influence on the internal flow field. Under

such conditions, hydraulic performance becomes highly sensitive to impeller and volute geometries, making coordinated geometric optimization essential for improving both performance and stability.

Previous studies have demonstrated the measurable influence of key geometric parameters on mini- and micro-centrifugal pump performance. Shigemitsu et al. [5] investigated the effects of blade outlet angle and blade thickness and showed that reducing blade thickness and appropriately increasing the blade outlet angle can improve head and efficiency within structural constraints. Khan et al. [6] examined low-specific-speed centrifugal pumps by reducing the volute throat area by 25% and 50%, and further reducing the volute gap width by 50%. Their results showed that throat-area reduction moved the best-efficiency point closer to the design flow rate and improved efficiency at underload and design conditions, while gap-width reduction shifted the head–capacity curve upward and improved hydraulic efficiency at design and overload conditions. Dong and Liu [7] optimized the impeller structure of a micro-centrifugal pump using pressure pulsation and shear stress as objectives, reporting a 40% reduction in the pressure-pulsation strength coefficient near the volute tongue and maximum shear-stress reductions of 42% in the impeller and 28% in the volute. These quantitative findings confirm that impeller and volute parameters strongly affect pump head, efficiency, and flow stability. However, many existing studies still focus on individual geometric factors or isolated component-level modifications, whereas the coupled influence of impeller and volute parameters has not been sufficiently explored within a systematic computational fluid dynamics (CFD)-based optimization workflow.

With the rapid development of computational resources, CFD has become an indispensable tool for resolving complex viscous flow structures in micro-centrifugal pumps. Compared with empirical correlations and simplified two-dimensional analytical models, CFD provides detailed information on pressure distribution, velocity fields, vortical structures, leakage flow, shear stress, and residence-time characteristics. Zhou et al. [8] investigated the influence of tip clearance on the performance of high-speed micro-pumps and showed that semi-open impeller micro-pumps are highly sensitive to tip-clearance variation, which strongly affects head and efficiency. Fraser et al. [9] reviewed the use of CFD in the development of ventricular assist devices and emphasized its value in assessing shear stress, residence time, hemolysis-related flow features, and hemocompatibility-related design risks. Parlak et al. [10] designed a mini double-discharge centrifugal pump and verified the CFD predictions experimentally, demonstrating the usefulness of CFD for evaluating dimensionless head and flow coefficients under multiphase-flow conditions. These studies indicate that CFD can effectively reveal internal flow mechanisms and support pump performance evaluation, but direct CFD-based design exploration remains computationally expensive when multiple geometric variables and performance objectives are involved.

To reduce the computational burden, CFD has increasingly been combined with design of experiments (DOE), surrogate modeling, and genetic algorithm (GA)-based optimization. Hou and Xue [11] performed multi-objective optimization of a miniature high-speed centrifugal pump and reported that, at the design condition of 10,000 rpm and 4.8 $m^3 \cdot h^{-1}$, the optimized pump achieved a head of 46.1 m and an efficiency of 49.7%; after optimization, the head increased by 3.7 m and the hydraulic efficiency improved by 4.8%. Their sensitivity analysis further identified the impeller outlet diameter and blade outlet angle as dominant variables affecting pump performance. İncebay and Yapici [12] combined an adaptive neuro-fuzzy inference system (ANFIS) surrogate with a GA to optimize hydraulic efficiency and hemolysis index in a centrifugal blood pump. Ghadimi et al. [13] used neural-network-based surrogate modeling and a GA to optimize the shape of a centrifugal blood pump

while considering hemolysis risk and hydraulic performance. Collectively, these studies demonstrate that surrogate-assisted optimization can improve pump performance and reduce computational cost. However, many studies still focus on specific pump types or selected performance objectives, while the integration of automated CFD simulation, surrogate-model validation, multi-objective optimization, and subsequent experimental flow-field verification remains insufficient.

Although CFD technology and multi-objective optimization algorithms have significantly improved the reliability and efficiency of centrifugal pump design, practical implementation still faces limitations such as insufficient workflow integration, frequent manual intervention, and inefficient data exchange between geometry generation, mesh generation, CFD solving, and optimization modules. To overcome these challenges, integrated CFD-optimization platforms have been developed to combine CFD simulation, parametric modeling, automated meshing, surrogate modeling, and design optimization into iterative design workflows [14,15]. For instance, Fu et al. [16] established a centrifugal pump optimization platform by coupling PUMPLINX CFD with UG software within MATLAB. Based on a comprehensive loss assessment model, the platform effectively enhanced the hydraulic efficiency and cavitation resistance of a fuel centrifugal pump. Similarly, Alawadhi et al. [17] constructed an integrated optimization environment by coupling five modules: ANSYS Vista CPD, a response surface optimizer, DesignModeler, ANSYS TurboGrid, and ANSYS CFX, which were associated with ANSYS Release 16.0 according to the cited study, to design and optimize the impeller and volute, thereby realizing a closed-loop process for erosion rate prediction and structural optimization. De Donno et al. [18] integrated Scilab 5.5.2, ANSYS CFX, and DAKOTA 6.8 to build an automated optimization framework for automotive engine-cooling pumps, enabling global design-variable sampling and optimization. The platform's performance was validated through mesh independence analysis and CFD simulations, demonstrating strong engineering applicability. In another study, Zhang et al. [19] developed radial basis function (RBF) metamodels for pump head, efficiency, and required net positive suction head, showing that RBF-based surrogate models could approximate CFD responses at test points and support multi-objective pump optimization. These studies demonstrate that integrated CFD-optimization platforms can improve automation, reduce repetitive manual operations, and enhance pump performance. However, many existing platforms remain primarily numerical or application-specific, and few studies combine automated CFD workflow construction, surrogate-model validation, multi-objective optimization, and experimental flow-field verification within a unified framework.

Building on this limitation, experimental validation is essential for assessing the engineering applicability of CFD-based optimization outcomes. In recent years, particle image velocimetry (PIV) has become an important tool for experimentally validating CFD analyses of centrifugal pumps because it can provide non-intrusive velocity field information inside transparent or optically accessible flow passages. Shigemitsu et al. [20] performed PIV measurements in a mini centrifugal pump with a 55 mm open impeller and clarified the velocity and vorticity distributions near the volute tongue, demonstrating the usefulness of PIV for revealing internal flow structures in mini pumps. Ni et al. [21] combined energy performance tests, PIV measurements, and CFD simulations to investigate the internal flow characteristics of a reactor coolant pump; within the main operating range of 0.8–1.2 times the design flow coefficient, the maximum error between the numerical and experimental energy performance was less than 10%, and the minimum error was below 0.1%. Tan et al. [22] integrated performance tests, PIV experiments, and numerical simulations to study vortex evolution in a single-blade centrifugal pump, reporting a head–flow performance error of 3.4% between simulation and experiment under a part-load flow

condition and revealing the role of jet–wake interaction near the volute tongue in vortex evolution. Černý and Polák [23] used PIV to measure the inlet pipe velocity field and evaluated the consistency between numerical and experimental results under different boundary conditions. Jiang et al. [24] combined computational fluid dynamics–discrete element method (CFD-DEM) simulation with high-speed photography and energy-characteristic experiments to analyze particle dynamics in a solid–liquid two-phase centrifugal pump, revealing the influence of inlet flow rate on flow pattern, energy performance, and particle motion. These studies show that experimental flow-field measurements can effectively complement CFD-based analysis by providing external-performance and internal-flow evidence. However, in many optimization-oriented studies, validation is still limited to external performance curves or isolated flow-field measurements, and the combined verification of optimized pump designs using both hydraulic performance tests and PIV-based internal-flow comparison remains insufficient.

Motivated by these developments, this study develops an integrated CFD-optimization platform for micro-centrifugal pumps that unifies parametric modeling, automated meshing, CFD solving, surrogate modeling, and Pareto-based multi-objective optimization into a closed-loop workflow. The optimized design is subsequently verified through hydraulic performance experiments and PIV flow-field measurements to assess the fidelity of numerical predictions. This approach aims to enhance design efficiency, reduce manual intervention, and strengthen consistency between simulation and experiment, thereby providing a reproducible methodology for high-fidelity design and optimization of micro-scale fluid-machinery components.

2. Numerical Simulation of the Micro-Centrifugal Pump

2.1. Development of the CFD Simulation–Optimization Platform

An integrated CFD simulation–optimization platform was developed to realize a closed-loop and fully automated workflow covering parametric design, geometric modeling, mesh generation, numerical computation, and multi-objective optimization. The platform employs parameter-driven control and script-based data exchange to overcome interoperability barriers among heterogeneous software environments. In this framework, any update to design variables automatically triggers geometry regeneration, mesh reconstruction, solver execution, and optimization iteration (Figure 1), thereby achieving unified management of geometric and physical parameters throughout the entire design process.

Technically, a hybrid orchestration strategy is implemented by coupling external Python scripting (Python 3.8) with the ANSYS Workbench 2020 R2 environment. The CFturbo API (CFturbo 2021.2.2) programmatically modifies key hydraulic design variables, including blade number, blade exit angle, and volute throat height, and exports the updated geometry. Supplementary solid modeling of non-hydraulic components (e.g., impeller hub, front and rear cover plates, and pump casing) is performed via the SolidWorks API (SolidWorks 2023), maintaining both assembly integrity and parametric controllability. The resulting flow passage is subsequently imported into ANSYS DesignModeler (DM) for secondary parameterization and geometric healing to ensure robust hand-off to the CFD solver.

High-quality structured or hybrid meshes are generated using ANSYS Meshing, and steady-state flow solutions are computed with ANSYS CFX, ensuring grid independence and numerical stability. For optimization, a Python-based module integrates optimal Latin hypercube sampling (OLHS), a Kriging surrogate model, and a multi-objective genetic algorithm (MOGA) to perform global design-space exploration and Pareto-front identification. Overall, the platform substantially improves automation, efficiency, and

reproducibility in the design of micro-centrifugal pumps, providing a coherent link between CFD simulation, experimental validation, and practical engineering application.

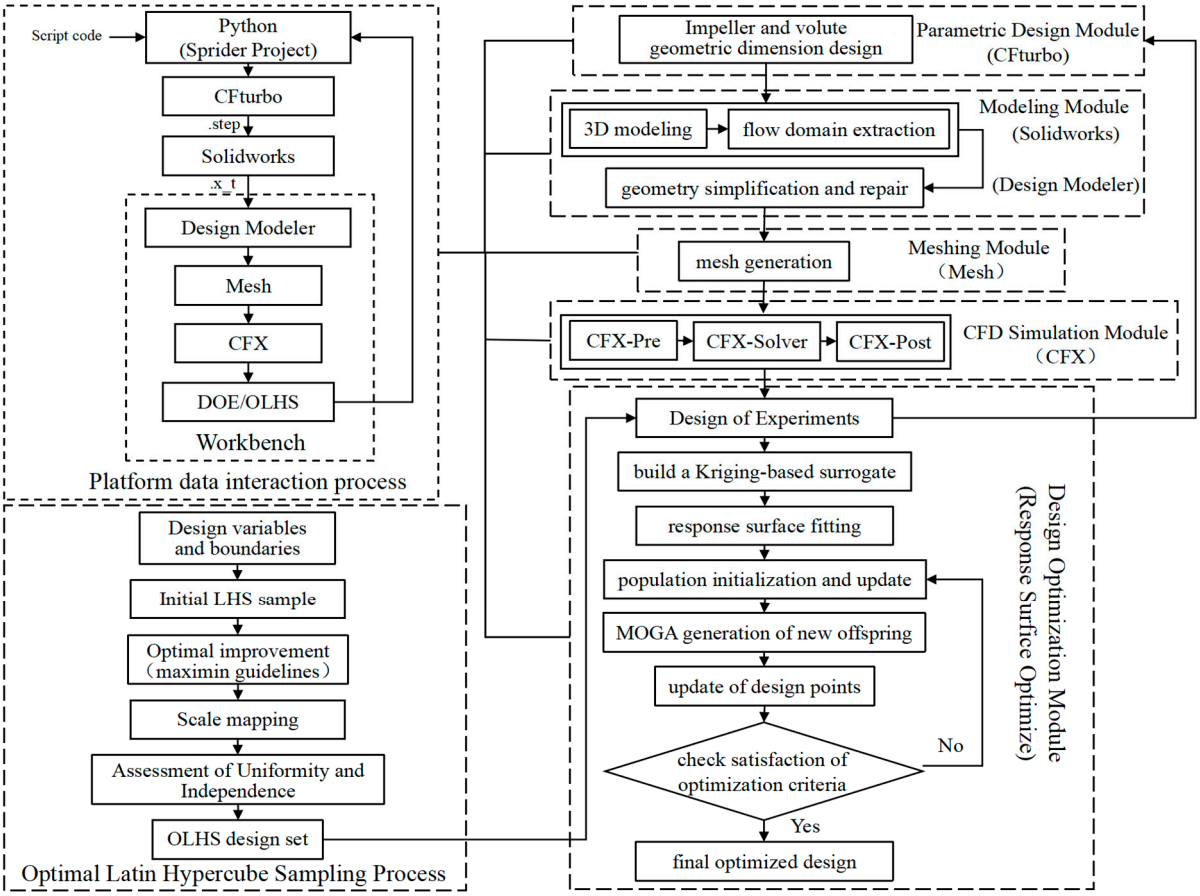


Figure 1. Workflow of the integrated CFD simulation–optimization platform.

2.2. Structural Design of Micro-Centrifugal Pump

2.2.1. Design Parameters

The investigated micro-centrifugal pump (MCP) was designed based on a three-dimensional scan of an existing prototype. The extracted geometric features were organized into a set of design parameters defining the hydraulic design point and the principal dimensions of the impeller and volute (Table 1).

Table 1. Basic design parameters of the MCP.

Parameter	Symbol	Design Value	Unit
Flow rate	Q	16	$L \cdot min^{-1}$
Head	H	4	m
Rotational speed	n	6000	rpm
Pump inlet diameter	D_{in}	14	mm
Impeller outlet diameter	D_2	38	mm
Blade thickness	d	2.0	mm
Impeller outlet width	b_2	2.0	mm
Impeller hub diameter	D_h	7.5	mm
Blade exit angle	β_2	25	°
Number of blades	Z	6	-
Volute base-circle diameter	D_3	40	mm
Pump outlet diameter	D_{out}	14	mm
Volute outlet length	L	50	mm

Table 1. *Cont.*

Parameter	Symbol	Design Value	Unit
Volute inlet width	b	3.9	mm
Volute throat height	h	6	mm
Cutwater angle	ϕ_0	25	°

2.2.2. Three-Dimensional Modeling

Using the integrated CFD simulation–optimization platform, a full three-dimensional model of the MCP was constructed (Figure 2). Compared with conventional single-software workflows, the present method resolves three persistent issues in the modeling process: (i) labor-intensive geometry reconstruction, (ii) unreliable parameter transfer, and (iii) insufficient fidelity in flow-passage extraction.

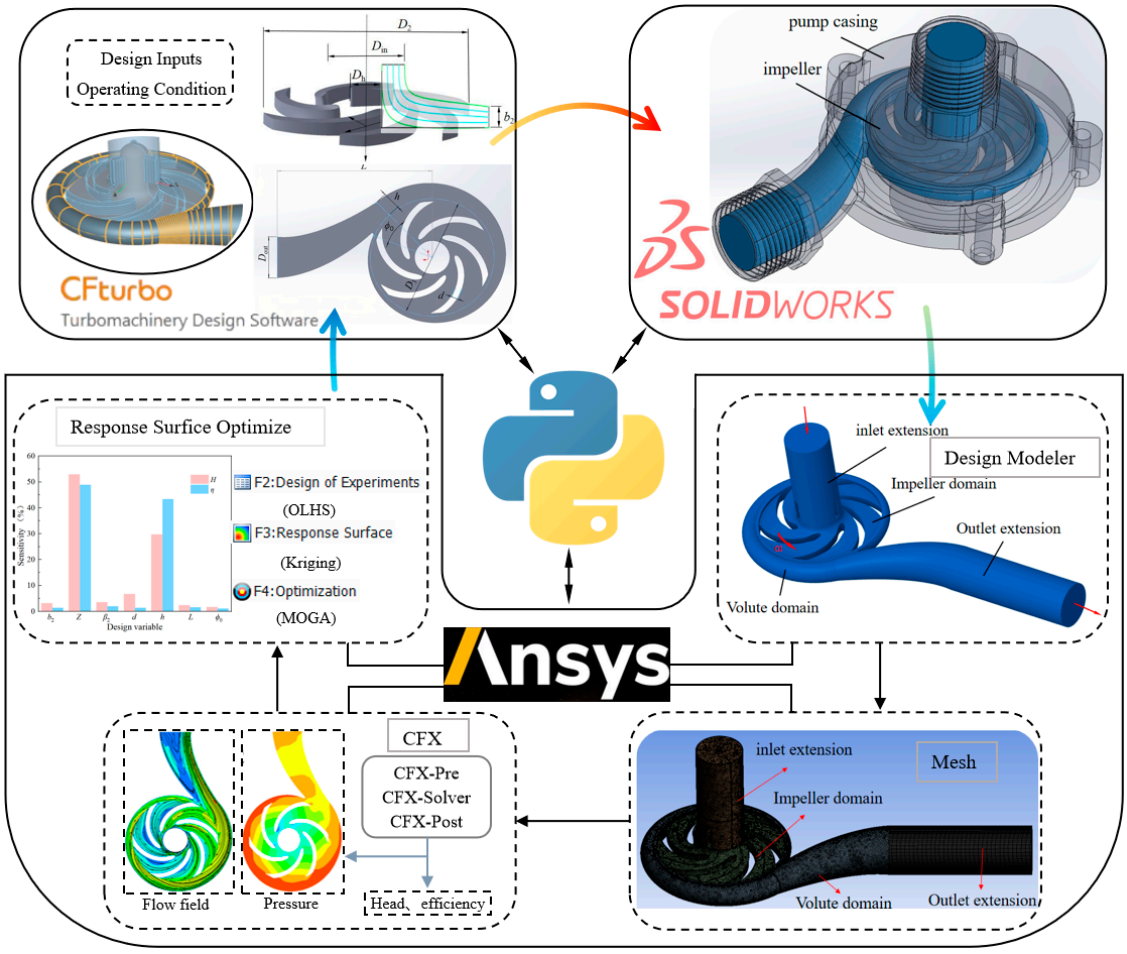


Figure 2. Schematic of the integrated CFD simulation–optimization platform. Black arrows indicate the main workflow and data-transfer links among the software modules, while colored arrows highlight key parameter and geometry-transfer routes. The central Python module coordinates parameter updating, geometry regeneration, meshing, CFD solving, and optimization.

The CFturbo module was employed to generate the impeller meridional profile and the preliminary volute geometry. Python scripts extracted and organized the governing design variables, enabling programmatic control and traceable parameter management. The parameter set was then imported into SolidWorks to construct non-hydraulic components (impeller hub, front/rear cover plates, and pump cover) while maintaining parametric linkages so that any change in hydraulic parameters automatically updates the complete

assembly. The resulting flow passages were subsequently transferred to ANSYS DesignModeler (DM) via external scripts for secondary parameterization and geometric healing. This step prevents defects and meshing failures commonly encountered during direct geometry import and ensures consistent geometry transfer to the CFD environment.

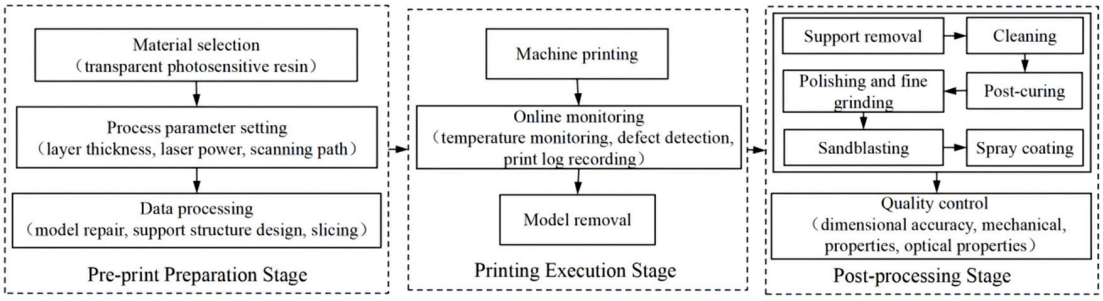
The established workflow achieves cross-platform synchronization and dynamic updating of both discrete variables (e.g., blade count) and continuous variables (e.g., exit angle, throat height). It thus provides a unified, stable, and reusable geometric foundation for subsequent CFD simulations and multi-objective optimization studies.

2.2.3. Experimental Model Fabrication

To validate the structural integrity and functional feasibility of the optimized design, a transparent prototype of the micro-centrifugal pump was fabricated using a high-precision stereolithography apparatus (SLA) 3D printing with a photosensitive resin (Table 2). Owing to the confined internal passages and the limited accessibility for post-processing, the impeller was divided into two segments and printed separately. The two parts were assembled using a mortise-and-tenon alignment combined with adhesive bonding to ensure high positional accuracy and maintain the geometric fidelity of the internal flow passages. The SLA process yielded excellent dimensional precision and optical transparency, providing favorable conditions for subsequent flow-field visualization experiments [25]. This digital manufacturing route significantly shortened the prototyping cycle and facilitated rapid iteration between design optimization and experimental validation. The overall 3D-printing workflow and the assembled prototype are illustrated in Figure 3. For the dynamic test stage, a contactless radial magnetic suspension drive was employed, utilizing stator–rotor magnetic coupling with rotor-mounted permanent magnets. This configuration enables impeller rotation and radial support without physical contact, effectively eliminating mechanical friction and associated parasitic losses. Consequently, it enhances operational stability, reliability, and durability during high-speed operation [26,27].

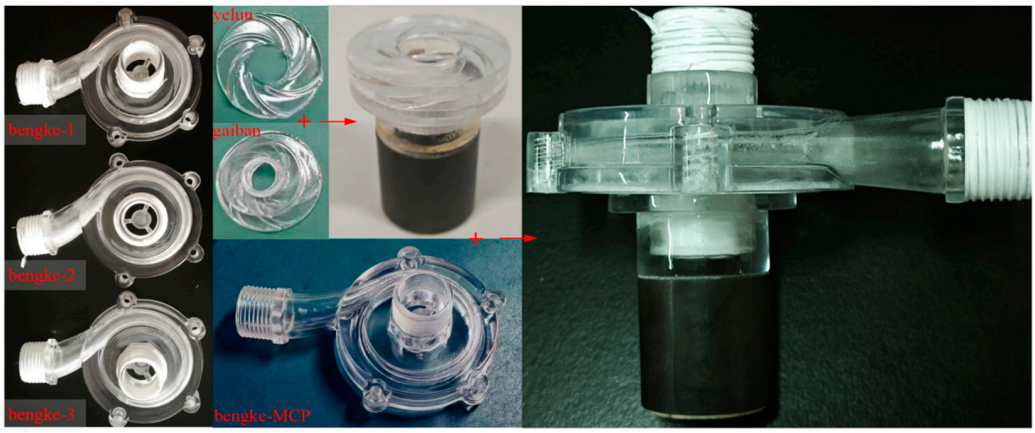
Table 2. List of 3D-printed components.

Component Name	Code	Description
MCP-Pump Casing	bengke-MCP	Pump casing of the MCP
MCP-Shroud	gaiban-MCP	Rear cover plate of the MCP impeller
MCP-Impeller	yelun-MCP	Integrated front cover plate and blades
Scheme 1-Pump Casing	bengke-1	Pump casing for optimization Scheme 1
Scheme 2-Pump Casing	bengke-2	Pump casing for optimization Scheme 2
Scheme 3-Pump Casing	bengke-3	Pump casing for optimization Scheme 3
Optimized-Shroud	gaiban	Optimized impeller rear cover plate
Optimized-Impeller	yelun	Optimized integrated front cover plate and blades



(**a**)

Figure 3. *Cont.*



(**b**)

Figure 3. 3D printing of the micro-centrifugal pump: (**a**) workflow of the 3D-printing process; (**b**) prototype of the micro-centrifugal pump. The red arrows indicate the assembly sequence from the printed components to the final prototype, and the plus signs indicate the combination of the impeller and cover-plate components.

2.3. CFD Numerical Simulation

2.3.1. Mesh Generation

Based on the flow-passage geometry derived from the integrated CFD simulation–optimization platform, a hybrid grid was generated for the computational domain using ANSYS Meshing. In regions with complex geometry, such as the inlet duct, impeller blade passages, and the volute near the cutwater, unstructured meshes with local refinement were applied to accurately resolve steep pressure and velocity gradients. In contrast, the outlet extensions, where the flow becomes more uniform, were discretized with structured hexahedral meshes to reduce computational cost while maintaining solution accuracy.

Because mesh resolution directly affects numerical accuracy and computational cost [28], a mesh independence test was conducted to determine a reasonable grid density, as shown in Figure 4. Several mesh schemes with different total cell numbers were generated by gradually reducing the local element size in the impeller passages, volute tongue region, and inlet/outlet extensions. For each mesh scheme, a steady-state computational fluid dynamics simulation was performed under the same operating conditions, boundary conditions, turbulence model, and convergence criteria. After convergence, the pump head and hydraulic efficiency were extracted and plotted against the total cell number. As the mesh was refined, both indicators gradually approached stable values. When the total cell number exceeded approximately 1.0×10^6, their variations became small, indicating that the main hydraulic performance parameters were essentially mesh-independent. Considering numerical accuracy, mesh quality, and computational cost, the final mesh containing 1,630,213 cells with a mean orthogonal quality (OQ) greater than 0.70 was selected for the subsequent simulations. Table 3 summarizes the mesh resolution in the three principal directions, where N_x, N_r, and N_θ denote the axial (streamwise), radial (hub-to-shroud or pipe radius), and circumferential (local radius) directions, respectively. The final meshing layout is illustrated in Figure 5.

Table 3. Mesh resolution in the three directions for the final model.

Region	N_x (Axial)	N_r (Radial)	N_θ (Circumferential)	Mesh Topology
Inlet extension	150	35	220	unstructured
Impeller domain	30	95	597	unstructured
Volute domain	250	30	597	unstructured
Outlet extension	200	35	220	structured

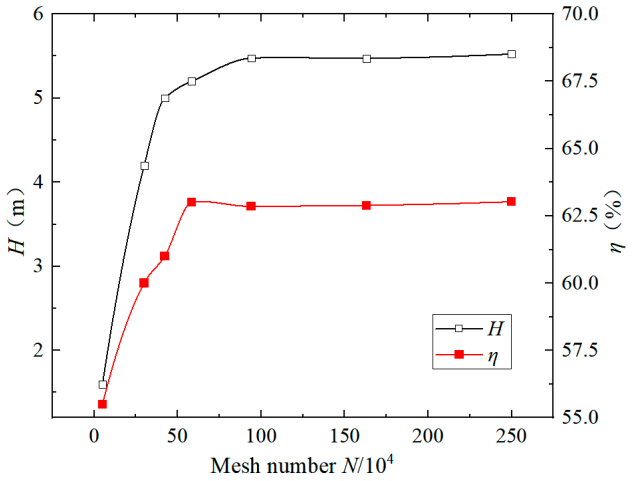


Figure 4. Results of the mesh independence study.

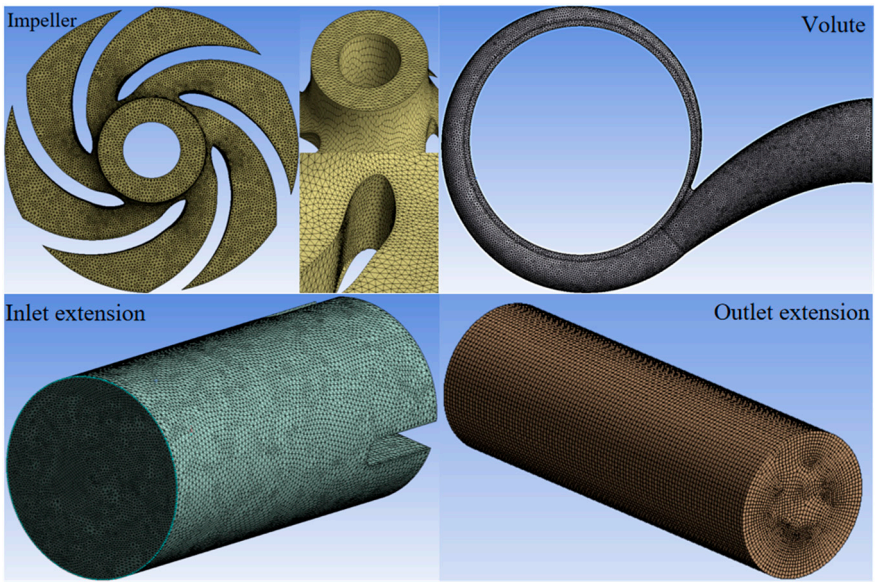


Figure 5. Meshing of the micro-centrifugal pump flow passage.

2.3.2. Boundary Conditions

The CFD simulations were performed for the full three-dimensional flow domain; therefore, the governing transport equations correspond to the three-dimensional incompressible steady Reynolds-averaged Navier–Stokes equations. The renormalization-group (RNG) *k*-ε turbulence model was employed owing to its improved capability in predicting swirling, rotating, and strongly curved flows typical of impeller passages and volute regions. Previous studies have demonstrated that, compared with the standard *k*-ε formulation, the RNG *k*-ε model provides superior accuracy for internal turbomachinery flows at comparable computational cost [29,30].

The three-dimensional incompressible steady Reynolds-averaged Navier–Stokes equations and the RNG *k*-ε turbulence-model equations are given as follows:

$$\frac{\partial(\rho u_i)}{\partial x_i} = 0, \frac{\partial(\rho u_i u_j)}{\partial x_j} = -\frac{\partial p}{\partial x_i} + \frac{\partial}{\partial x_j}\left[(\mu + \mu_t)\left(\frac{\partial u_i}{\partial x_j} + \frac{\partial u_j}{\partial x_i}\right)\right] \quad (1)$$

$$\frac{\partial(\rho k u_j)}{\partial x_j} = \frac{\partial}{\partial x_j}\left[\left(\mu + \frac{\mu_t}{\sigma_k}\right)\frac{\partial k}{\partial x_j}\right] + P_k - \rho\varepsilon \quad (2)$$

$$\frac{\partial(\rho\varepsilon u_j)}{\partial x_j} = \frac{\partial}{\partial x_j}\left[\left(\mu + \frac{\mu_t}{\sigma_k}\right)\frac{\partial k}{\partial x_j}\right] + C_{1\varepsilon}\frac{\varepsilon}{k}P_k - C_{2\varepsilon}\rho\frac{\varepsilon^2}{k} - R_\varepsilon \quad (3)$$

with closures

$$\mu_t = \rho C_\mu \frac{k^2}{\varepsilon},\ P_k = \mu_t(2S_{ij}S_{ij}),\ S_{ij} = \frac{1}{2}\left(\frac{\partial u_i}{\partial x_j} + \frac{\partial u_j}{\partial x_i}\right) \quad (4)$$

and the RNG correction term

$$R_\varepsilon = \rho C_\mu \eta^3\left(1 - \frac{\eta_{\mathrm{RNG}}}{\eta_0}\right)\frac{\varepsilon^2}{k(1+\beta\eta_{\mathrm{RNG}}^3)},\ \eta_{\mathrm{RNG}} = \frac{Sk}{\varepsilon},\ S = \sqrt{2S_{ij}S_{ij}} \quad (5)$$

where u_i is the time-averaged velocity component; x_i is the spatial coordinate; p is the mean pressure; ρ is the fluid density; μ and μ_t are the molecular and eddy viscosities, respectively; P_k is the production of turbulent kinetic energy by mean shear; and σ_k, σ_ε, C_μ, $C_{1\varepsilon}$, $C_{2\varepsilon}$, η_0, and β are model constants; η_{RNG} is the RNG dimensionless strain parameter; and R_ε denotes the RNG correction term in the ε-equation.

In ANSYS CFX, the governing equations were discretized using the finite-volume method. The momentum and continuity equations were solved with the CFX coupled solver, while the k and ε transport equations were iteratively coupled with the mean-flow equations through the eddy viscosity formulation.

The working fluid was water at 25 °C, treated as incompressible and isothermal. A mass–flow inlet of 0.26619 kg·s^{-1} (corresponding to the design flow rate) was prescribed, and a static-pressure outlet of 1 bar was imposed. The impeller region was modeled as a rotating reference frame at 6000 rpm, while the remaining zones were stationary. Rotor-stator interaction was handled using the Frozen-Rotor frame-change model. This quasi-steady treatment was used for comparative hydraulic performance prediction during the surrogate-based optimization, and the same relative rotor-stator angular position was maintained for all simulated designs. However, transient jet–wake interaction near the volute tongue cannot be fully resolved by the Frozen-Rotor model; therefore, the present CFD results should be interpreted as quasi-steady predictions rather than fully time-resolved unsteady-flow simulations. All solid boundaries were set as no-slip walls. Standard wall functions were adopted for near-wall treatment, with prism-layer inflation to maintain y^+ values within the valid range [31,32]. Steady RANS iterations proceeded until all residuals fell below 10^{-5}, and monitored global quantities (head and efficiency) reached convergence, ensuring numerical stability and repeatability.

To assess the reliability of the CFD model, several quality-control criteria were considered, including mesh independence verification, mesh orthogonal quality, near-wall treatment, residual convergence, and stabilization of monitored head and efficiency. In addition, the CFD predictions were further evaluated through hydraulic performance measurements and PIV-based flow-field comparison. These procedures were used to ensure that the numerical model could reasonably capture the main hydraulic behavior of the micro-centrifugal pump.

2.3.3. Numerical Simulation Analysis

CFD simulations were conducted to analyze the internal flow field of the MCP and to obtain detailed pressure and velocity distributions within the impeller and volute on the $r-\theta$ plane ($z = 0$), as shown in Figure 6. Within the impeller domain, the static pressure increases continuously along the radial direction, reaching a maximum of approximately 1.142×10^5 Pa near the blade trailing edge. A distinct pressure difference between the pressure and suction sides at equal radii indicates significant blade loading and a strong radially outward pressure gradient responsible for head generation. Upon exiting the impeller, the pressure distribution in the volute becomes circumferentially non-uniform,

with a high-pressure region forming near the tongue due to jet–wake interaction and impingement, while the remaining volute regions exhibit relatively uniform pressure recovery. This pattern corresponds to classical centrifugal pump flow behavior and suggests additional mixing losses and potential sources of pressure pulsation.

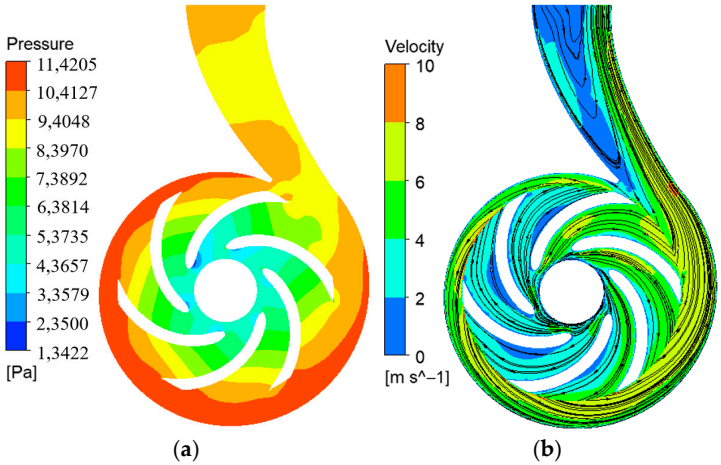


Figure 6. Static-pressure and velocity fields within the impeller and volute passages of the MCP: (**a**) static-pressure contours; (**b**) velocity-magnitude contours with streamlines.

The velocity field shows that the relative velocity is low near the impeller inlet and increases radially owing to centrifugal acceleration, attaining a peak of approximately 10 m·s^{-1} near the blade exit. As the flow enters the volute, the mean absolute velocity decreases due to the expanding cross-sectional area, indicative of diffusive deceleration. Low-velocity layers are also observed adjacent to the volute wall from the tongue to the outlet, attributed to viscous boundary-layer effects and secondary flow structures.

3. Multi-Objective Optimization Design

3.1. Selection of Design Variables and Objectives

To improve the hydraulic performance of the micro-centrifugal pump (MCP) without altering its external envelope, a parametric optimization of key impeller and volute geometrical parameters was performed. The impeller variables include the blade outlet width (b_2), blade number (Z), blade exit angle (β_2), and blade thickness (d). The volute variables comprise the throat height (h), outlet length (L), and tongue setting angle (ϕ_0). The baseline values, variation ranges, and increments of all variables are listed in Table 4. The present optimization focused on the primary impeller–volute hydraulic geometry. Gap-related parameters, such as side clearances between the impeller and housing and leakage paths, were not included as design variables in this stage. Considering both manufacturability and structural integrity of the micro-impeller, a coupling constraint ($b_2 = d$) was imposed during optimization. This ensures a continuous outlet cross-section and balances hydraulic capacity with mechanical stiffness.

The primary performance metrics for a micro-centrifugal pump are head (H) and hydraulic efficiency (η) [33,34]. In this study, both are taken as maximization objectives in the multi-objective optimization process.

The head quantifies the energy transferred to the fluid under the rated operating condition. For the CFD simulations, the pump head was evaluated using the area-averaged total pressure difference between the outlet and inlet:

$$H = \frac{p_2 - p_1}{\rho g} \tag{6}$$

where p_1 and p_2 are the area-averaged total pressures at the outlet and inlet, respectively (Pa), ρ is the fluid density (kg·m^{-3}), and g is the gravitational acceleration (m·s^{-2}).

Table 4. Optimization variables and bounds.

Component	Variable	Symbol	Initial Value	Range	Increment	Unit
Impeller	Outlet width	b_2	2.0	1.8–2.2	0.1	mm
	Blade count	Z	6	5–7	1.0	-
	Blade exit angle	β_2	25	22–28	1.0	°
	Blade thickness	d	2.0	1.8–2.2	0.1	mm
Volute	Throat height	h	6.0	4–8	1.0	mm
	Outlet length	L	50	45–55	1.0	mm
	Tongue setting angle	ϕ_0	25	20–30	1.0	°

The efficiency reflects the energy-conversion capability of the MCP and is given by

$$\eta = \frac{P_e}{P} = \frac{\rho g Q H}{M\omega} \tag{7}$$

where P_e and P denote the output and input power (W), Q is the flow rate (m^3·s^{-1}), M is the input torque (N·m), and ω is the angular velocity (rad·s^{-1}).

3.2. Optimization Methods and Workflow

3.2.1. Optimal Latin Hypercube Sampling (OLHS)

To construct a surrogate model that maps the geometric design vector x to the pump performance responses $\{H, \eta\}$, a space-filling design of experiments (DOE) was first generated within the normalized design space defined by the lower and upper bounds of the variables. An effective DOE improves the space-filling property of the samples, reduces sample clustering, and enables the surrogate model to capture nonlinear input–output dependencies with a limited number of CFD evaluations [35,36].

Conventional sampling methods, such as Central Composite Design (CCD) and Box–Behnken Design (BBD), are well-suited to second-order polynomial regression but tend to cluster points near the coordinate axes or the design center. This characteristic limits their suitability for global exploration in highly nonlinear design spaces. Latin hypercube sampling (LHS) improves spatial coverage by stratifying each variable dimension, yet it does not ensure uniform inter-point spacing, and its projections may still exhibit non-uniform clustering in some subregions.

To overcome these drawbacks, the optimal Latin hypercube sampling (OLHS) technique was employed. OLHS begins with an initial LHS configuration and iteratively adjusts sample positions to maximize the minimum pairwise distance between points (maximin criterion) while enforcing projection uniformity. This optimization yields a more evenly distributed sampling plan, minimizing variable correlations and enhancing the surrogate model's predictive generalization.

The optimization objective for OLHS is expressed as

$$\max D = \min_{i \neq j} \sqrt{\sum_{k=1}^{n} \left(x_{ik} - x_{jk} \right)^2} \tag{8}$$

where x_{ik} represents the normalized coordinate of the i sample in the k design variable, and n is the number of design dimensions. The goal is to maximize the minimum Euclidean distance D among all sample pairs, thereby ensuring uniform dispersion of design points within the multidimensional space.

Figure 7 conceptually compares several DOE strategies, illustrating that OLHS provides superior space-filling and projection-uniformity characteristics. Figure 8 presents the OLHS sample distribution under multiple design variables; the points are uniformly dispersed across the global design space with no evident clustering, adequately representing the joint characteristics of the variables. Table 5 summarizes the CFD results corresponding to the OLHS designs, supplying the dataset for subsequent surrogate modeling and multi-objective optimization.

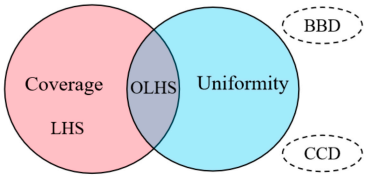


Figure 7. Conceptual comparison of four DOE schemes in terms of coverage and uniformity.

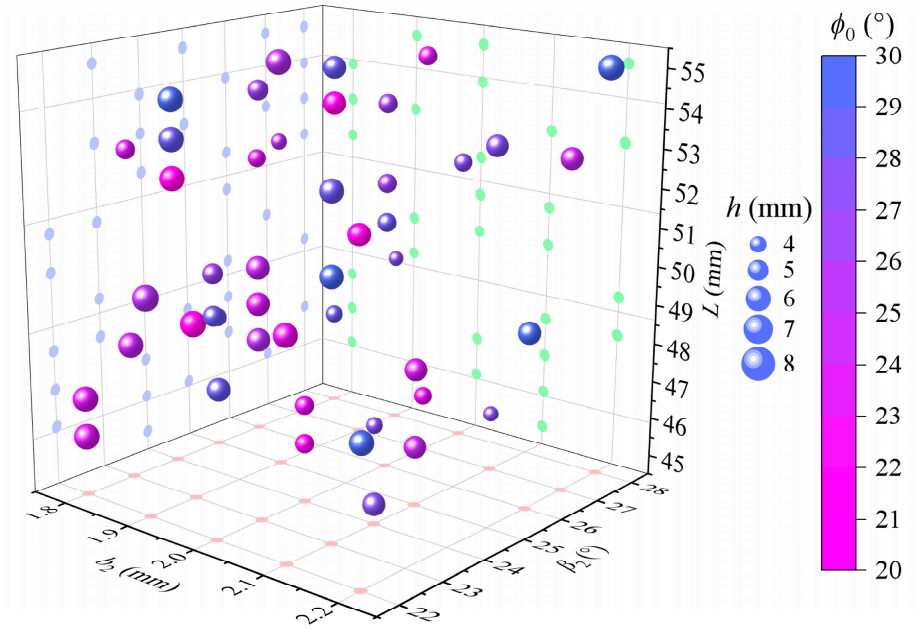


Figure 8. Distribution of samples generated by optimal Latin hypercube sampling (OLHS). The light-colored points on the coordinate planes represent projections of the design samples onto the corresponding two-dimensional planes, providing a visual reference for their spatial distribution.

Table 5. Selected OLHS design points and corresponding CFD evaluation results.

No	b_2 (mm)	Z	d (mm)	β_2 (°)	h (mm)	L (mm)	ϕ_0 (°)	H (m)	η (%)
1	2.2	7	2.2	28	8	55	30	7.57	75.3
2	2	5	2	24	6	47	22	5.29	62.4
3	2.1	6	2.1	25	7	48	23	6.76	73.9
4	1.8	7	1.8	26	8	49	24	7.02	76.0
5	2	7	2	28	6	52	27	6.38	68.0
6	2.1	5	2.1	23	7	53	28	6.24	71.7
7	1.8	6	1.8	24	8	54	29	6.61	75.5
8	2	6	2	27	6	46	22	5.63	63.4
9	1.8	5	1.8	23	8	48	24	6.26	75.8
10	2	5	2	26	6	51	27	5.38	62.7
⋮	⋮	⋮	⋮	⋮	⋮	⋮	⋮	⋮	⋮
50	1.8	6	1.8	22	8	47	23	6.61	76.2

Note: Only selected design points are shown for brevity.

3.2.2. Kriging Response Surface Model

Response surface modeling provides a compact representation of the input–output relationship for complex systems and is widely employed in design optimization, sensitivity analysis, and uncertainty quantification [37,38]. Typical surrogate models include polynomial regression, Kriging (Gaussian process) models, and neural-network approximations. In this work, a Kriging surrogate was trained using the OLHS design points and their corresponding CFD-computed responses. Because of its spatial interpolation nature, Kriging captures both global trends and local correlations, offering high accuracy for nonlinear, multi-modal responses [39,40].

In this study, the Kriging model was used to approximate the relationship between the design vector $x = [b_2, Z, \beta_2, d, h, L, \phi_0]$ and the hydraulic responses of the micro-centrifugal pump. The responses were the pump head H and hydraulic efficiency η, which were obtained from CFD simulations of the OLHS design points. Accordingly, two independent Kriging surrogate models were constructed for $H(x)$ and $\eta(x)$, respectively.

The Kriging predictor can be written as

$$Y(x) = \sum_{i=1}^{m} \beta_i \, f_i(x) + z(x) \tag{9}$$

where $Y(x)$ is the predicted response, representing either $H(x)$ or $\eta(x)$ in the present work; β_i are the regression coefficients; $f_i(x)$ denotes the regression basis function that describes the global trend of the response surface; and $z(x)$ is a zero-mean Gaussian process used to model local nonlinear deviations and spatial correlation among the sample points. The regression basis $f_i(x)$ may be a constant or a low-order polynomial term, depending on the Kriging formulation. Thus, the first term in Equation (9) represents the global approximation of pump performance, whereas $z(x)$ corrects the local deviation based on the correlation structure of the OLHS-CFD samples.

The covariance between two sample points, x_i and x_j, is

$$Cov\left[z(x_i), z(x_j)\right] = \sigma^2 R\,(x_i, x_j) \tag{10}$$

where σ^2 is the process variance and $R\,(x_i, x_j)$ is the correlation kernel.

A Gaussian (squared-exponential) kernel was adopted:

$$R(x_i, x_j) \; = exp\left(- \sum_{k\,=1}^{p} \theta_k \left| x_i^k - x_j^k \right|^2 \right) \tag{11}$$

where θ_k denotes the inverse squared length-scale for the k design dimension. The hyperparameters $\{\theta_k\}$ are determined via maximum likelihood estimation (MLE), after which the Best Linear Unbiased Predictor (BLUP) and its prediction variance are obtained analytically.

The surrogate accuracy was assessed using the coefficient of determination R^2 [41]:

$$R^2 = 1 - \frac{\sum_{i\,=1}^{n} \left(y_i - \hat{y}_i\right)^2}{\sum_{i\,=1}^{n} \left(y_i - \overline{y}\right)^2} \tag{12}$$

where $\hat{y}_i$ are surrogate predictions, y_i are CFD-derived values, and $\overline{y}$ is the sample mean. Values of R^2 close to 1 indicate high explanatory power.

Because Kriging is an interpolation-based model, a near-perfect R^2 on learning points may occur under noise-free training data and does not by itself guarantee out-of-sample predictive reliability. Therefore, the predictive error was further quantified using cross-validation. For a K-fold cross-validation, the sample set is partitioned into K mutually exclusive subsets. At fold k, the surrogate is trained on the remaining samples and evaluated

on the held-out verification subset, yielding verification errors $e_i^{(k)} = y_i - \hat{y}_i^{(-k)}$. The cross-validated RMSE and MAE are defined as

$$\mathrm{RMSE_{CV}} = \sqrt{\frac{1}{N}\sum_{k=1}^{K}\sum_{i\in V_k}\left(e_i^{(k)}\right)^2}, \mathrm{NAE_{CV}} = \frac{1}{N}\sum_{k=1}^{K}\sum_{i\in V_k}\left|e_i^{(k)}\right| \quad (13)$$

where V_k denotes the index set of verification samples in fold k. The leave-one-out (LOO) scheme is a special case with $K = N$, in which each sample is predicted by a surrogate trained on the remaining $N - 1$ samples.

Figure 9 presents the accuracy assessment of the Kriging surrogate model. As shown in Figure 9a, the Kriging predictions on the learning points agree closely with the CFD observations and are distributed along the 45° line, with $R^2 = 1$. This result indicates an almost residual-free fit of the training samples, which is typical for an interpolation-based Kriging model using noise-free CFD data. However, the learning-point fit alone does not fully reflect the out-of-sample predictive capability of the surrogate model. Therefore, the cross-validation prediction–observation differences for head and hydraulic efficiency were further plotted as a function of the observation point, as shown in Figure 9b. The prediction-observation differences were calculated as the cross-validation predictions minus the corresponding CFD observations. Thus, H_{error} represents the head error in meters, whereas η_{error} represents the hydraulic-efficiency error in percentage points. The error distributions generally fluctuate around zero, although relatively larger deviations are observed at several points. These localized deviations may be related to stronger nonlinear responses in certain regions of the design space and the limited number of CFD samples available for surrogate construction. Nevertheless, the overall error metrics summarized in Table 6 indicate that the Kriging model provides acceptable predictive accuracy for surrogate-assisted optimization.

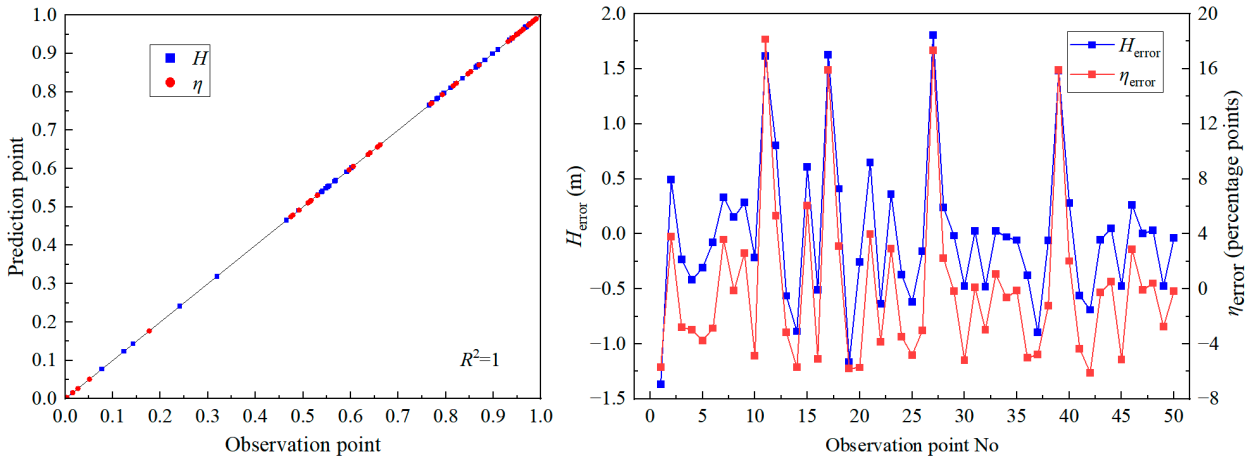


Figure 9. Accuracy assessment of the Kriging surrogate model: (**a**) prediction–observation comparison on the learning points and (**b**) cross-validation prediction–observation differences as a function of the observation point.

Table 6. Cross-validation prediction errors of the Kriging surrogate model.

Output Variable	Cross-Validation Scheme	RMSE	MAE	MAPE (%)
Head, H (m)	5-fold cross-validation	0.652 m	0.470 m	8.28%
Efficiency, η (%)	5-fold cross-validation	5.85%	4.14%	6.55%

Using the trained Kriging surrogate, the influence of each design variable on pump head H and efficiency η was quantified via a one-at-a-time (OAT) local sensitivity analysis (Figure 10). In this approach, sensitivities are evaluated at a selected reference point x_0: for each variable x_i, all other variables are fixed at x_0, while x_i is varied within its prescribed bounds to generate a one-dimensional surrogate response curve $\hat{y}(x_i)$. The raw local sensitivity is defined as the signed relative output variation along this curve.

$$S_i = \mathrm{sgn}\left(\frac{d\hat{y}}{dx_i}\right)\frac{max(\hat{y}) - min(\hat{y})}{Avg(\hat{y})} \tag{14}$$

where $\hat{y}$ denotes the surrogate-predicted output (H or η). For percentage presentation, the sensitivities are normalized as

$$S_i^{(\%)} = 100\% \times \frac{|S_i|}{\sum_{j=1}^{n}|S_j|} \tag{15}$$

This metric provides an interpretable screening measure of variable importance at x_0; it is local and does not explicitly separate interaction effects.

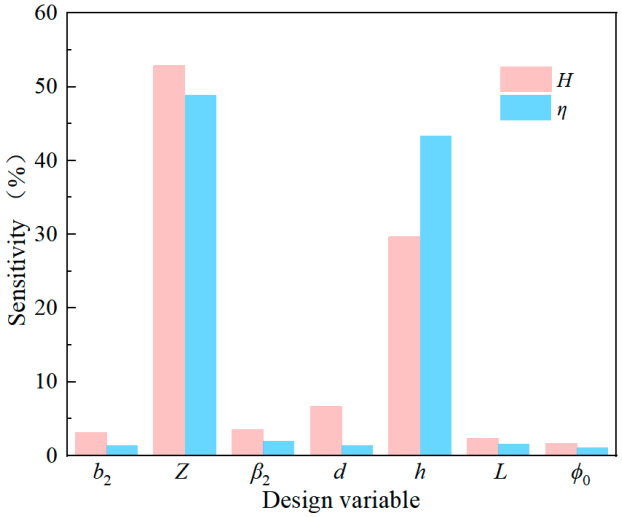


Figure 10. Sensitivity of design variables to head and efficiency.

As shown in Figure 10, the blade count Z and volute throat height h are the two most influential variables for both H and η. Specifically, Z accounts for 52.9% of the normalized sensitivity for H and 48.9% for η, while h accounts for 29.7% for H and 43.4% for η. The remaining variables exhibit comparatively smaller normalized sensitivities within the investigated design ranges. The importance ranking for H is $d > \beta_2 > b_2 > L > \phi_0$; for η, it is $\beta_2 > L > b_2 \approx d > \phi_0$.

To further clarify these effects, single-factor sweeps were conducted for Z and h (Figure 11). Both variables exhibit nonlinear correlations with hydraulic performance within the explored bounds. As Z increases, H and η improve up to $Z = 7$, beyond which the benefit saturates. For h, both metrics first decrease and then rise, attaining maxima at $h = 8$ mm. These behaviors highlight the critical role of Z and h in governing blade loading and diffusion characteristics. Pairwise interaction effects were then evaluated for two variable pairs with moderate main effects (Figure 12): (b_2, d) and (β_2, L). When d is at a high level, increasing b_2 leads to marked gains in both H and η, evidencing a positive synergy between passage width and structural thickness. In contrast, at high β_2, extending L causes H and η to decrease first and then increase, reflecting a trade-off between diffusion effectiveness and circumferential non-uniformity in the volute.

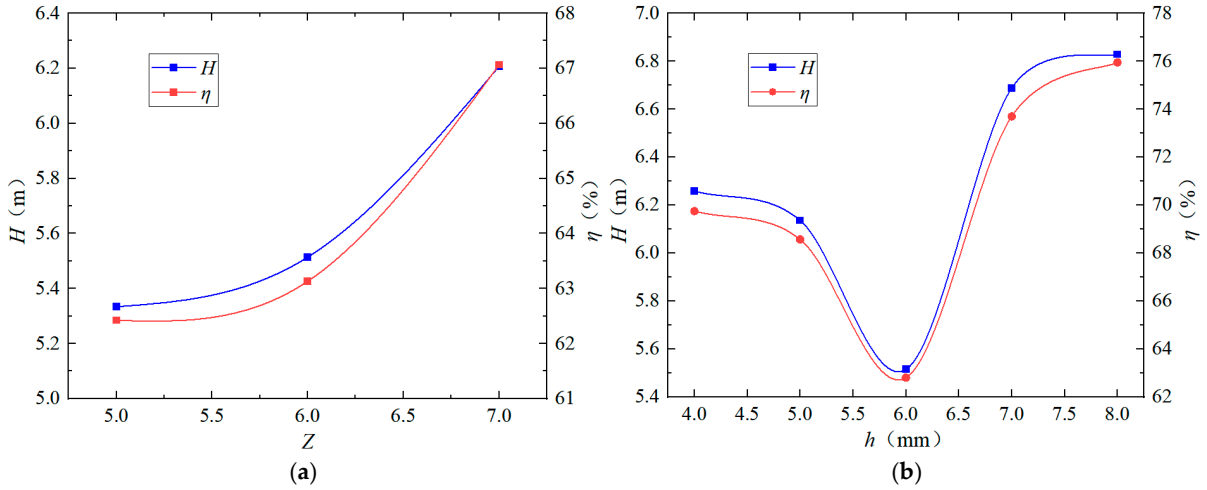


Figure 11. Single-factor effects: (**a**) head and efficiency versus blade count Z; (**b**) head and efficiency versus throat height h.

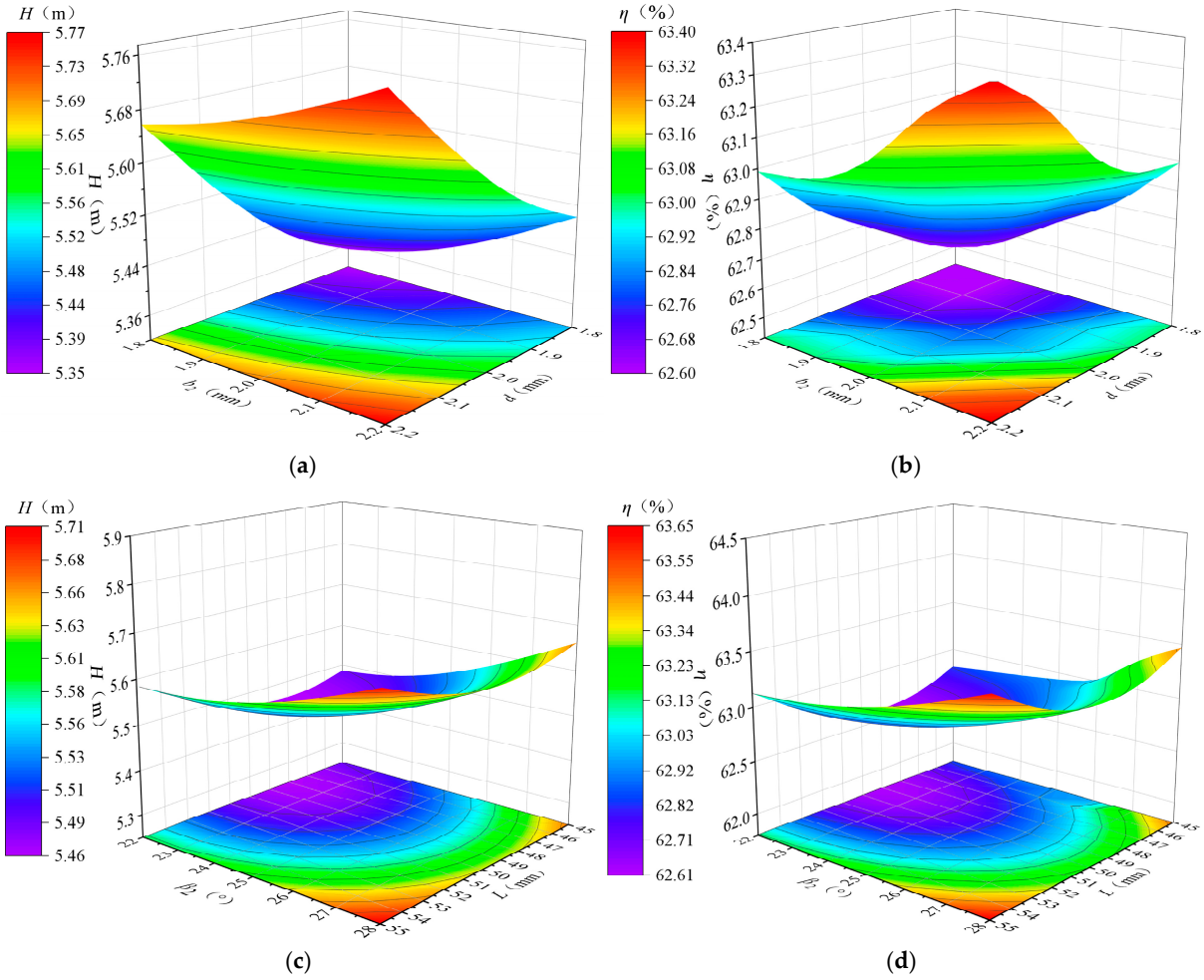


Figure 12. Kriging response surface maps: (**a**) (b_2, d)→H; (**b**) (b_2, d)→η; (**c**) (β_2, L)→H; and (**d**) (β_2, L)→η.

Overall, within the explored design space, blade count and throat height emerge as the most influential parameters, with optimal values of Z = 7 and h = 8 mm. Significant interactions are also observed for (b_2, d) and (β_2, L). These findings guide the subsequent genetic algorithm search, which concentrates sampling density around the high-performance regions identified by the surrogate analysis.

3.2.3. Multi-Objective Genetic Algorithm (MOGA)

The multi-objective genetic algorithm (MOGA) extends the classical genetic algorithm to handle multiple, potentially conflicting objectives. It uses non-dominated sorting and diversity-preserving mechanisms (e.g., crowding distance) to approximate the Pareto front while balancing convergence and diversity, making it well suited to surrogate-based optimization when CFD evaluations are expensive [42]. In this study, the Kriging surrogates of head (H) and efficiency (η) serve as the objective functions.

The optimization model can be expressed as

$$var\ x = [b_2, Z, d, h, L, \phi_0] \tag{16}$$

$$obj\begin{cases}\max f_\delta(H)\\ \max f_\delta(\eta)\end{cases} \tag{17}$$

$$s.t\begin{cases}1.8\ \text{mm} \le b_2 \le 2.2\ \text{mm}\\ 5 \le Z \le 6\\ 22^\circ \le \beta_2 \le 28^\circ\\ 1.8\ \text{mm} \le d \le 2.2\ \text{mm}\\ 4\ \text{mm} \le h \le 6\ \text{mm}\\ 45\ \text{mm} \le L \le 55\ \text{mm}\\ 20^\circ \le \phi_0 \le 30^\circ\end{cases} \tag{18}$$

where H is the head, η is the efficiency, and b_2, Z, β_2, d, h, L, and ϕ_0 are the blade outlet width, blade count, blade outlet angle, blade thickness, throat height, outlet length, and tongue setting angle, respectively.

The MOGA search was performed on the trained Kriging surrogate with the following configuration: an initial population of 10,000 individuals to ensure broad genetic diversity; 2000 offspring per generation to balance exploration and efficiency; and a maximum of 20 generations to terminate the evolution after convergence. Infeasible geometries violating design constraints were penalized by assigning reduced fitness scores to suppress their propagation in subsequent iterations. Upon reaching convergence, a set of non-dominated solutions (forming the Pareto front) was obtained. From this front, three candidate Pareto solutions were selected to represent the head-dominant, efficiency-dominant, and compromise-performance designs, respectively, enabling flexible engineering choices based on specific application requirements [43,44]. Table 7 compares the baseline and optimized designs. Relative to the baseline MCP (head = 5.55 m; efficiency = 63.02%), the three optimized candidates achieve head increments of 2.23 m, 2.21 m, and 2.28 m, corresponding to efficiency improvements of 14.52%, 14.63%, and 14.12%, respectively. These results confirm that the surrogate-assisted MOGA framework significantly enhances the hydraulic performance of the MCP while delivering multiple high-performance design alternatives to accommodate diverse engineering requirements.

Table 7. Comparison of optimization results for the micro-centrifugal pump.

Case	b_2 (mm)	Z	d (mm)	β_2 (°)	h (mm)	L (mm)	ϕ_0 (°)	H (m)	η (%)
MCP	2	6	2	25	6	50	25	5.55	63.02
Scheme 1	2.2	7	2.2	28	8	45	30	7.78	77.54
Scheme 2	2.2	7	2.2	28	8	45	29	7.76	77.65
Scheme 3	2.2	7	2.2	28	8	46	29	7.83	77.14

3.3. Optimization Results and Performance Evaluation

Figure 13 compares the hydraulic characteristics of the baseline MCP and the three optimized candidates. Across the entire tested flow range, all optimized configurations exhibit higher head and efficiency than the baseline. Among them, Scheme 1 consistently delivers the highest head throughout the operating domain, particularly in the low- to mid-flow regions. It also maintains the broadest high-efficiency plateau, achieving a peak efficiency of 77.54% with minimal off-design deterioration as the flow rate increases. This indicates superior flow adaptability and energy-conversion effectiveness. Schemes 2 and 3 remain competitive at high flow rates but show narrower efficiency plateaus and greater performance variation across the full operating window. Considering head improvement, peak efficiency, and curve smoothness, Scheme 1 demonstrates the most balanced and robust overall performance.

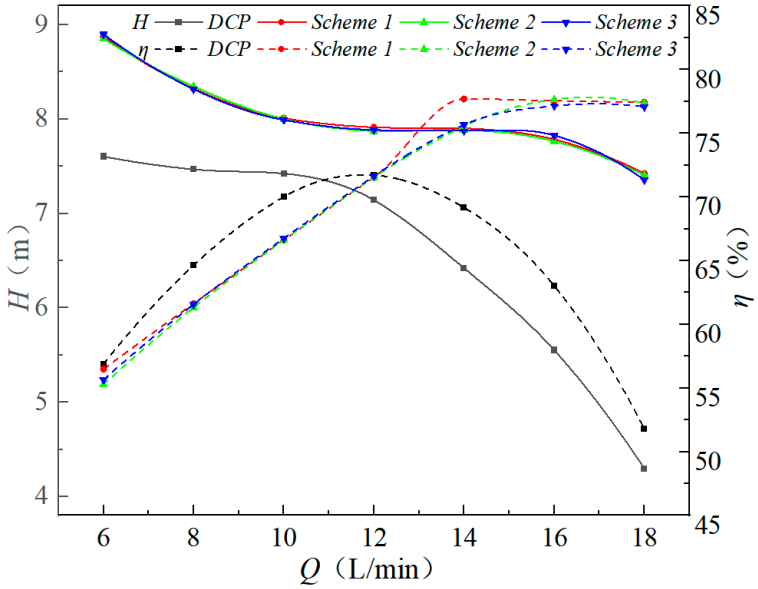


Figure 13. Hydraulic performance curves of the baseline and optimized micro-centrifugal pumps.

Figure 14 presents the simulated static-pressure distribution on the mid-plane ($r - \theta$, $z = 0$) for the optimized micro-centrifugal pump. Compared with the baseline, the optimized designs yield a more uniform pressure field at the volute outlet and smoother pressure gradients within the impeller passages, implying improved diffusion and reduced local losses. In particular, Scheme 1 shows the most homogeneous pressure at the impeller exit and minimal high-pressure accumulation near the volute tongue. Scheme 2 exhibits a slightly lower overall pressure level and notable circumferential non-uniformity, whereas Scheme 3 approaches the mean pressure of Scheme 1 but retains residual non-uniformity at the impeller outlet and within the volute, suggesting a less stable diffusion process. Figure 15 displays the corresponding mid-plane velocity-magnitude contours with streamlines. The optimized geometries effectively suppress low-velocity regions near the volute outlet and produce more coherent streamline organization compared with the baseline. Scheme 1 exhibits the most uniform discharge at the impeller exit, minimal recirculation near the tongue, and a continuous, well-aligned flow direction through the volute. Scheme 2 achieves partial improvement but retains local flow deviation, whereas Scheme 3 still presents discernible recirculation and separation zones. Overall, the optimized flow structures demonstrate enhanced uniformity, reduced secondary flow intensity, and improved diffusion continuity, features that are most pronounced in Scheme 1 and consistent with its superior hydraulic performance curves.

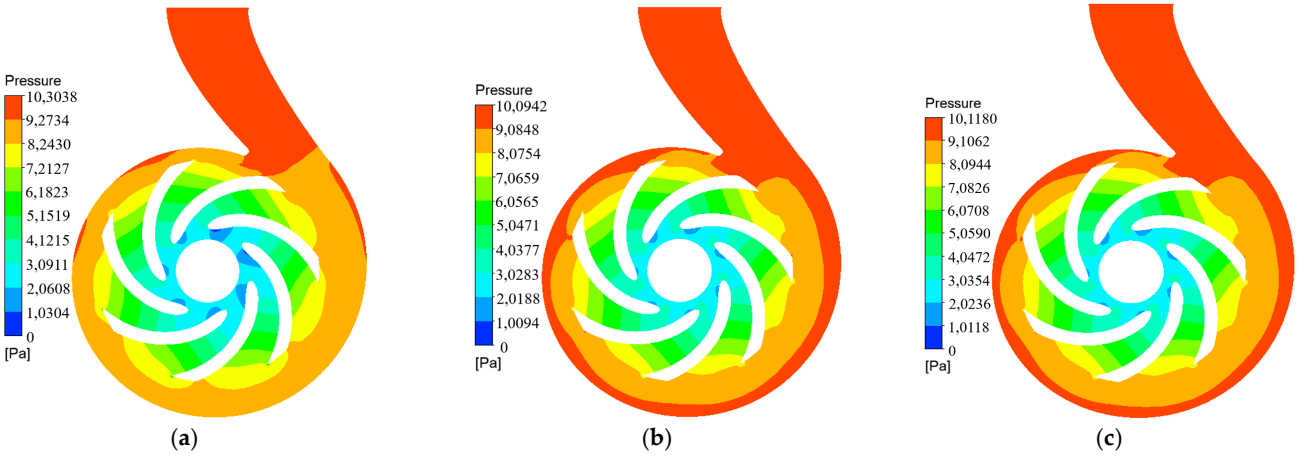


Figure 14. Mid-plane static-pressure contours for the optimized micro-centrifugal pump: (**a**) Scheme 1; (**b**) Scheme 2; and (**c**) Scheme 3.

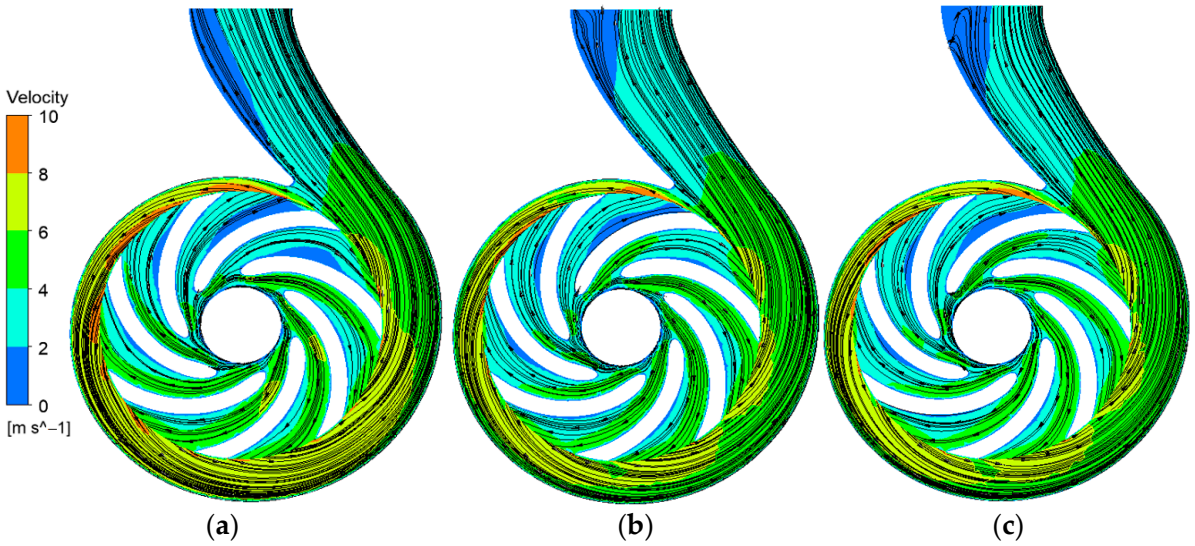


Figure 15. Mid-plane velocity-magnitude contours with streamlines for the optimized micro-centrifugal pump: (**a**) Scheme 1; (**b**) Scheme 2; and (**c**) Scheme 3.

4. Experimental Validation

4.1. Experimental Platform Setup

To validate the optimized design and assess the fidelity of the CFD predictions, a dedicated centrifugal pump test rig was constructed at the Shanghai Institute of Technology for hydraulic performance and particle image velocimetry (PIV) measurements. Before each test, the pump and pipeline were fully primed to eliminate entrained air and ensure complete flooding of the casing, thereby securing measurement accuracy and stable operation [45,46]. The pump rotational speed was regulated by a motor controller, and the operating points across a range of flow rates and heads were obtained by adjusting the downstream valve while monitoring flow and pressure in real time. The schematic of the closed-loop test system is shown in Figure 16, the physical layout in Figure 17, and the principal instruments in Table 8. Hydraulic performance data were acquired using a digital turbine flowmeter and pressure sensors, while PIV measurements employed a continuous-wave laser and a high-speed CMOS camera to capture tracer-particle motion in the transparent test section. Velocity fields were reconstructed from particle displacements using cross-correlation image processing.

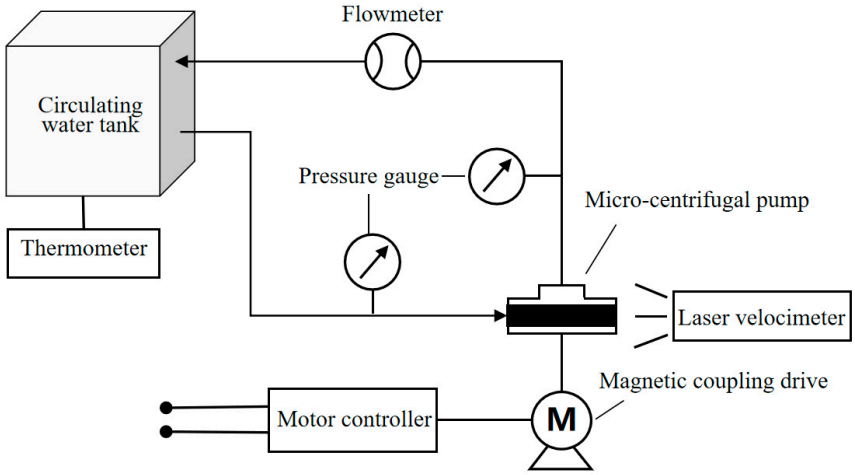


Figure 16. Schematic diagram of the centrifugal pump test loop.

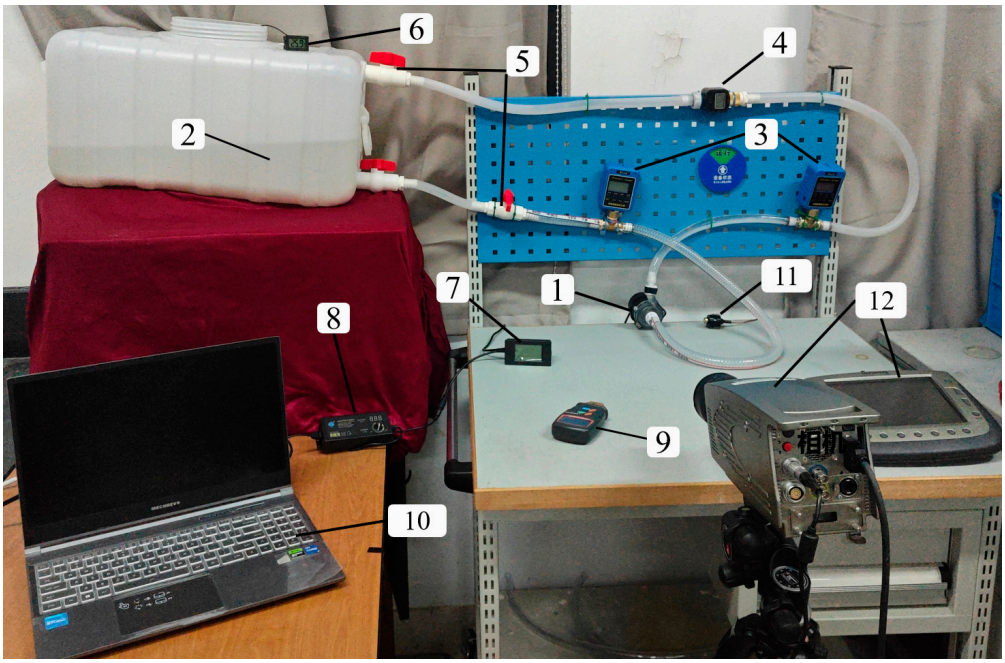


Figure 17. Experimental platform for hydraulic performance and PIV measurements. 1—centrifugal pump; 2—reservoir; 3—pressure gauge; 4—flowmeter; 5—valve; 6—thermometer; 7—digital multi-function meter; 8—motor controller; 9—laser tachometer; 10—computer; 11—continuous-wave laser; and 12—CMOS camera.

Table 8. Principal instruments used in the centrifugal pump experiments.

Instrument	Model	Key Specifications	Manufacturer (City, Country)
Controller	*MCP*-2460C	3–24 V (0.1 V)	Jizhao Technology Co., Ltd. (Zhongshan, China)
Flowmeter	*JCAG*0005	1–45.0 L·min^{-1} (0.1 L·min^{-1})	Geekercs Technology Co., Ltd. (Xuzhou, China)
Pressure gauge	*A*50 (*NPT* 1/8)	−0.1–5 MPa (0.0001 MPa)	Yinpin Electronic Apparatus Co., Ltd. (Hangzhou, China)
Multifunction power meter	*PZEM*-051	6.5–100 V, 0–100 A	Peacefair Electronic Technology Co., Ltd. (Ningbo, China)
Laser tachometer	*DT*-2234C+	2.5–9999 rpm (0.1 rpm)	Chenzhou Technology Co., Ltd. (Shenzhen, China)

Table 8. *Cont.*

Instrument	Model	Key Specifications	Manufacturer (City, Country)
Thermometer	*JX-XH*	−50–110 °C (0.1 °C)	Foshan Chuannuo Ceramic Machinery Co., Ltd. (Foshan, China)
Continuous-wave laser	*HB*400-*PWM*	532 nm, 400 mW	Shenzhen Chaonai Digital Technology Co., Ltd. (Shenzhen, China)
CMOS camera	*i-SPEED* 3	1280 × 1024 px 15,000 fps	iX Cameras Ltd. (Rochford, United Kingdom)

4.2. Experimental Design and Operating Procedure

4.2.1. Hydraulic Performance Test

The hydraulic performance test evaluated the flow–head characteristics of the pump before and after optimization under a range of operating conditions [47]. The motor speed was controlled at discrete values from 2500 rpm to 3500 rpm using a frequency converter. For each speed, the downstream valve was gradually adjusted to span the entire operating range, and at least three repeated measurements were recorded at every operating point to ensure repeatability. For the hydraulic performance test, the experimental head was calculated from the measured pressure difference between the inlet and outlet pressure taps, with elevation correction included when applicable. The pressure taps were arranged at approximately the same elevation as far as possible to minimize the influence of the elevation difference. The CFD-predicted head was evaluated using the total pressure difference as defined in Equation (6). The corresponding flow–head (*Q*-*H*) curves were then constructed from the measured data. Test conditions (working fluid: water at 25 °C) and the measurement locations were kept consistent with the CFD setup to enable direct comparison.

4.2.2. Particle Image Velocimetry (PIV) Test

For the PIV measurements, a representative operating condition of 3000 rpm and 7 L·min^{-1} was selected for validation. A continuous-wave laser was shaped into a light sheet with an approximate thickness of 1 mm to illuminate the mid-plane cross-section at the volute outlet ($r - \theta$ plane, $z = 0$), thereby enhancing particle scattering and image contrast. Tracer-particle motions were recorded using a high-speed camera (i-speed 3) at 2000 fps with a field of view of 60 mm and an effective image resolution of 1280 × 1024 pixels. The spatial calibration factor was defined as

$$s = \frac{60}{N_{\mathrm{px}}}\ \mathrm{mm/pixel} \tag{19}$$

where $N_{\mathrm{px}} = 1280$ is the effective image width in pixels. The flow was first recorded as a video sequence, and consecutive frames were extracted in Phantom Camera Control (PCC v3.11) for PIV processing. Image pairs were constructed using adjacent-frame pairing with a time separation of $\Delta t = 1/2000 = 0.5$ ms, yielding a set of image pairs for velocity statistics.

Velocity vectors were computed in PIVLab (MATLAB R2022a) using cross-correlation. To improve the correlation peak quality and spatial resolution, a multi-pass window-deformation scheme was adopted, with a final interrogation window size of 32 × 32 pixels. The seeding level was adjusted through preliminary trials to obtain an average particle image density of approximately 8–12 particle images per final interrogation window, thereby ensuring reliable cross-correlation. Vector quality control was performed using standard procedures, including peak ratio validation and median filtering, to identify and replace spurious vectors. The resulting velocity fields were then post-processed and

visualized in Tecplot 360 EX (2022 R1) to obtain the mean velocity-vector distribution on the $r - \theta$ plane (z = 0) at the volute outlet, thereby characterizing the cross-sectional flow structure. Figure 18 shows a representative PIV image-processing procedure, including the raw particle image in the illuminated measurement region, the selected region of interest (ROI), and the reconstructed velocity-vector field obtained by cross-correlation processing.

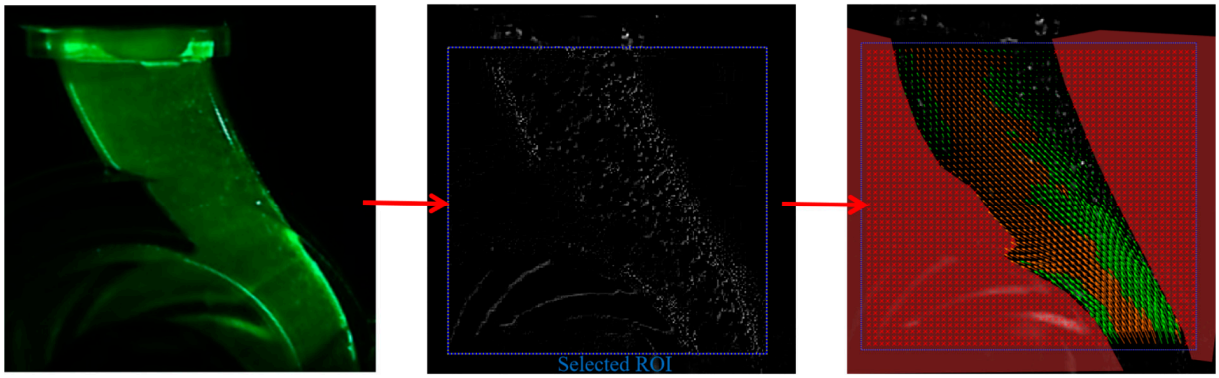


Figure 18. Representative PIV image-processing procedure at the volute outlet on the $r - \theta$ plane (z = 0): (**a**) raw particle image in the illuminated measurement region; (**b**) selected region of interest (ROI) used for cross-correlation analysis; and (**c**) reconstructed velocity-vector field obtained from PIVLab processing. The red arrows indicate the processing sequence, the blue dotted frame denotes the selected ROI, and the colors in panel (**c**) represent velocity magnitude.

4.3. Experimental Results and Validation

4.3.1. Hydraulic Performance Analysis

Figure 19 compares the experimental and CFD-predicted flow–head characteristics of the baseline MCP and the three optimized designs under multiple rotational speeds. The measured heads are slightly lower than the CFD predictions, which may be associated with manufacturing tolerances, possible leakage through small clearances, and measurement uncertainty under real test conditions. Despite these unavoidable practical factors, the overall deviation between simulation and experiment remains below 10%, indicating that the experimental results provide a meaningful validation of the CFD-predicted flow–head trends. Across all speeds and flow rates, the three optimized schemes consistently outperform the baseline pump, exhibiting higher heads and stable operation. The close agreement between the CFD and experimental trends supports the reliability of the numerical model for head prediction and the effectiveness of the surrogate-based optimization framework.

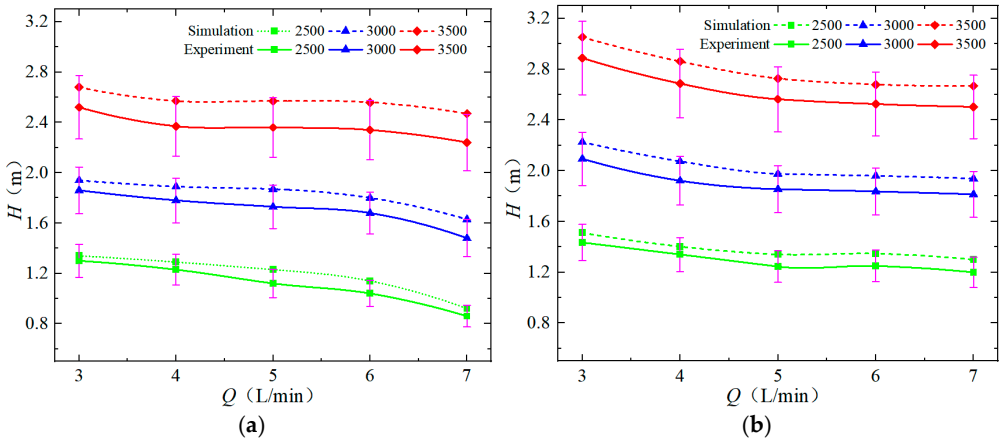


Figure 19. *Cont.*

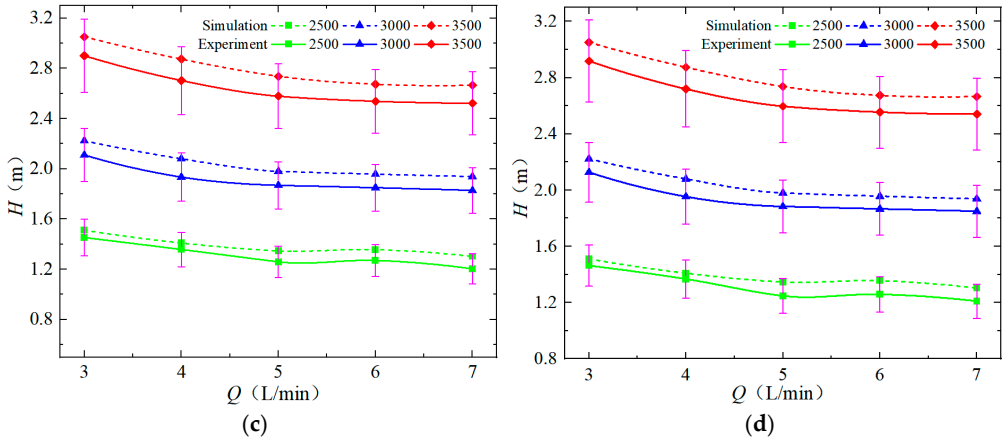


Figure 19. Flow–head characteristic curves for the MCP and optimized schemes: (**a**) MCP; (**b**) Scheme 1; (**c**) Scheme 2; and (**d**) Scheme 3.

4.3.2. Comparison of PIV Measurements and Numerical Simulations

Figures 20 and 21 compare the numerically simulated and experimentally measured velocity fields at the volute outlet on the $r - \theta$ plane (z = 0) under 3000 rpm for the micro-centrifugal pump before and after optimization. The CFD predictions and PIV measurements exhibit close agreement at both the cutwater (tongue) region and the volute outlet. The two methods show consistent global velocity distributions and principal velocity-gradient trends along the main passage, confirming the reliability of the CFD solution. A detailed comparison of the corresponding panels (a–d) in Figures 20 and 21 reveals a slight discrepancy near the tongue and on the left side of the volute outlet. In the PIV results, a distinct recirculation vortex observed in the CFD field is not clearly visible in the mean velocity map. This difference is mainly attributed to depth-averaging effects caused by the finite laser-sheet thickness and to non-phase-locked time averaging, during which counter-rotating velocity components partially cancel, reducing the apparent intensity of localized recirculation on a single cross-section.

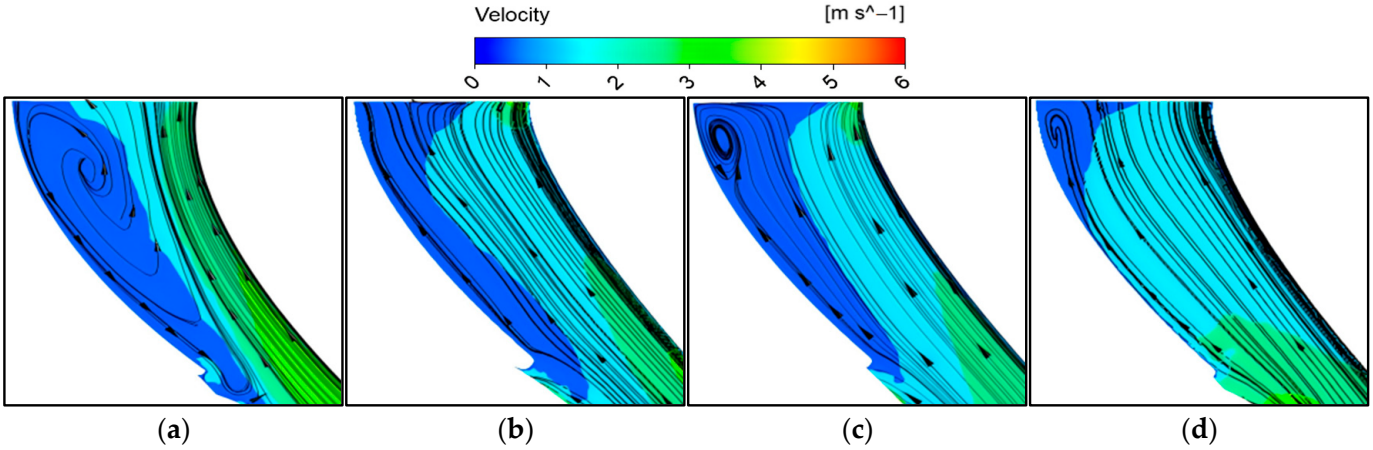


Figure 20. CFD-predicted velocity-magnitude contours with streamlines at the volute outlet on the $r - \theta$ plane (z = 0): (**a**) MCP; (**b**) Scheme 1; (**c**) Scheme 2; and (**d**) Scheme 3.

The combined evidence from hydraulic performance measurements and PIV/CFD field comparisons indicates consistent agreement in both the integral metric (head) and internal flow organization. The optimized configurations, particularly Scheme 1, exhibit improved diffusion uniformity and reduced recirculation near the tongue, consistent with the experimentally verified gains in head and efficiency.

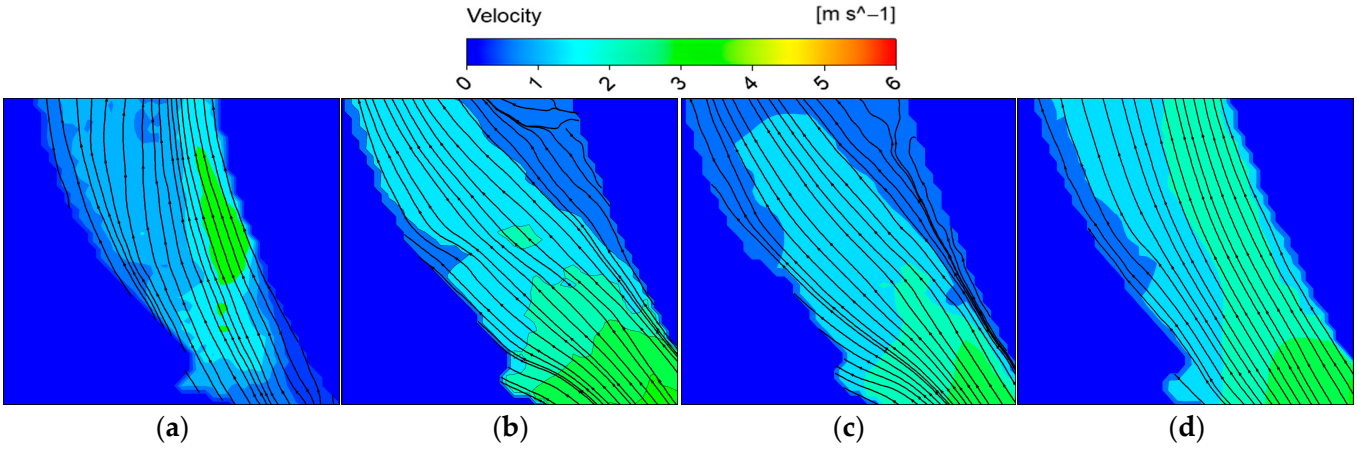


Figure 21. PIV-measured velocity-magnitude contours with streamlines at the volute outlet on the $r - \theta$ plane ($z = 0$): (**a**) MCP; (**b**) Scheme 1; (**c**) Scheme 2; and (**d**) Scheme 3.

5. Conclusions

This study developed an integrated CFD-optimization platform implementing a closed-loop workflow comprising parametric modeling, automated meshing, steady CFD solving, and surrogate-assisted multi-objective optimization. By combining optimal Latin hypercube sampling (OLHS), a Kriging response surface surrogate, and a multi-objective genetic algorithm (MOGA), coordinated tuning of key geometric parameters, particularly the blade count (Z) and volute throat height (h), was achieved. Relative to the baseline MCP, the optimized configurations attained average improvements of 40.36% in head and 22.89% in hydraulic efficiency. Among the optimized candidates, Scheme 1 exhibited the most favorable trade-off between head and efficiency across the entire operating range. Experimental validation confirmed the numerical results: the CFD-predicted heads deviated from measurements by less than 10% over all tested operating points, and PIV measurements corroborated the simulated velocity field structures and gradients near the volute outlet. These findings substantiate the fidelity and robustness of the proposed modeling and optimization framework. The developed platform provides a reproducible and extendable workflow for performance-oriented design of micro-centrifugal pumps, and more broadly, other types of small-scale turbomachinery requiring geometry-performance co-optimization.

Author Contributions: X.W.: Writing—review and editing, Funding acquisition, Project administration, Resources. H.W.: Writing—original draft, Visualization, Validation, Software, Methodology, Investigation, Formal analysis, Data curation. Y.X.: Writing—review and editing, Supervision, Conceptualization. All authors have read and agreed to the published version of the manuscript.

Funding: This research received no external funding.

Data Availability Statement: The data presented in this study are available on request from the corresponding author.

Acknowledgments: The authors gratefully acknowledge the Shanghai Institute of Technology for providing the laboratory facilities and experimental equipment that enabled this research.

Conflicts of Interest: The authors declare no conflicts of interest.

Nomenclature

k	Turbulent kinetic energy ($m^2 \cdot s^{-2}$)	P_e	Output power (W)
ε	Turbulent dissipation rate ($m^2 \cdot s^{-3}$)	P	Input power (W)
μ_t	Eddy viscosity (Pa·s)	Q	Flow rate ($m^3 \cdot s^{-1}$)

P_k	Production of turbulent kinetic energy by mean shear ($m^2 \cdot s^{-3}$)	Δz	Elevation difference between outlet and inlet (m)
$C_{1\varepsilon}$, $C_{2\varepsilon}$	Empirical constants	M	Input torque (N·m)
α_k, α_ε	Diffusion coefficients	D	Minimum pairwise distance in normalized design
η_0, β	RNG model constants	ω	Angular velocity (rad·s^{-1})
C_μ	Eddy viscosity constant	$Y(x)$	Surrogate prediction
η_{RNG}	RNG dimensionless strain parameter	β_i	Regression coefficients
ρ	Fluid density (kg·m^{-3})	$f_i(x)$	Polynomial basis functions
μ	Molecular viscosity (Pa·s)	$z(x)$	Zero-mean Gaussian process term
N_x	Mesh resolution in axial/streamwise	σ^2	Process variance
N_r	Mesh resolution in radial	p	Input dimension
N_θ	Mesh resolution in circumferential direction	θ_k	Dimension-wise length scale hyperparameters
H	Pump head (m)	R^2	Coefficient of determination
η	Hydraulic efficiency (%)	$\hat{y}_i$	Surrogate predictions
p_1, p_2	Inlet/outlet static pressure (Pa)	y_i	CFD-derived values
g	Gravitational acceleration (m·s^{-2})	$\overline{y}$	Sample mean

References

1. Al-Halhouli, A.; El Far, B.; Albagdady, A.; Al-Faqheri, W. Development of Active Centrifugal Pump for Microfluidic CD Platforms. *Micromachines* **2020**, *11*, 140. [CrossRef] [PubMed]
2. Li, K.; Xu, W.; Dou, H.-S. Flow Stability in a Miniature Centrifugal Pump under the Periodic Pulse Flow. *Energies* **2021**, *14*, 8338. [CrossRef]
3. Zhou, M.; Qi, Z.; Xia, Z.; Li, Y.; Ling, W.; Yang, J.; Yang, Z.; Pei, J.; Wu, D.; Huo, W.; et al. Miniaturized soft centrifugal pumps with magnetic levitation for fluid handling. *Sci. Adv.* **2021**, *7*, eabi7203. [CrossRef]
4. Yazdanpanah-Ardakani, K.; Niroomand-Osculi, H.; Sahebi-Kuzeh Kanan, R.; Shokri, N. Optimization of a centrifugal blood pump designed using an industrial method through experimental and numerical study. *Sci. Rep.* **2024**, *14*, 7443. [CrossRef] [PubMed]
5. Shigemitsu, T.; Fukutomi, J.; Kaji, K. Influence of Blade Outlet Angle and Blade Thickness on Performance and Internal Flow Conditions of Mini Centrifugal Pump. *Int. J. Fluid Mach. Syst.* **2011**, *4*, 317–323. [CrossRef]
6. Khan, M.F.; Gjernes, T.; Guenther, N.; Hickey, J.-P. Impact of Volute Throat Area and Gap Width on the Hydraulic Performance of Low-Specific-Speed Centrifugal Pump. *Modelling* **2024**, *5*, 659–672. [CrossRef]
7. Dong, X.; Liu, Y. Optimization design of the impeller structure for a micro centrifugal pump based on pressure pulsation and shear stress analysis. *Proc. Inst. Mech. Eng. Part A J. Power Energy* **2025**, *239*, 609–623. [CrossRef]
8. Zhou, H.; Xue, R.; Liang, Y.; Niu, B.; Chen, S.; Hou, Y. Tip clearance influence on the performance of high-speed micro-pumps. *Phys. Fluids* **2024**, *36*, 115129. [CrossRef]
9. Fraser, K.H.; Taskin, M.E.; Griffith, B.P.; Wu, Z.J. The use of computational fluid dynamics in the development of ventricular assist devices. *Med. Eng. Phys.* **2011**, *33*, 263–280. [CrossRef] [PubMed]
10. Parlak, Z.; Kemerli, M.; Engin, T.; Koç, Y. Design of a Mini Double-Discharge Centrifugal Pump under Multiphase Flow by CFD and Experimental Verification. *J. Appl. Fluid Mech.* **2018**, *11*, 1437–1448. [CrossRef]
11. Hou, Y.; Xue, R. Hydraulic Performance and Flow Characteristics of a High-Speed Centrifugal Pump Based on Multi-Objective Optimization. *Fluids* **2025**, *10*, 174. [CrossRef]
12. İncebay, Ö.; Yapici, R. Optimization of a centrifugal blood pump in terms of hemolysis index and hydraulic efficiency. *J. Braz. Soc. Mech. Sci. Eng.* **2024**, *46*, 5185. [CrossRef]
13. Ghadimi, B.; Nejat, A.; Nourbakhsh, S.A.; Naderi, N. Shape optimization of a centrifugal blood pump by coupling CFD with metamodel-assisted genetic algorithm. *J. Artif. Organs* **2018**, *22*, 29–36. [CrossRef]
14. Si, Q.; Lu, R.; Shen, C.; Xia, S.; Sheng, G.; Yuan, J. An Intelligent CFD-Based Optimization System for Fluid Machinery: Automotive Electronic Pump Case Application. *Appl. Sci.* **2020**, *10*, 366. [CrossRef]
15. Chen, L.; Yang, Y.; Song, X.; Zhang, X.; Gong, Y. Integrated optimization design of multiphase pump based on adaptive sparse grid method. *Ocean Eng.* **2024**, *298*, 117235. [CrossRef]
16. Fu, J.; Zhong, S.; Liu, X.; Zhao, C. Optimization design of aviation centrifugal pump based on synthetical loss model. *Proc. Inst. Mech. Eng. Part G J. Aerosp. Eng.* **2025**, *239*, 909–931. [CrossRef]
17. Alawadhi, K.; Alzuwayer, B.; Mohammad, T.A.; Buhemdi, M.H. Design and Optimization of a Centrifugal Pump for Slurry Transport Using the Response Surface Method. *Machines* **2021**, *9*, 60. [CrossRef]

18. De Donno, R.; Fracassi, A.; Ghidoni, A.; Morelli, A.; Noventa, G. Surrogate-Based Optimization of a Centrifugal Pump with Volute Casing for an Automotive Engine Cooling System. *Appl. Sci.* **2021**, *11*, 11470. [CrossRef]
19. Zhang, Y.; Wu, J.; Zhang, Y.; Chen, L. Design Optimization of Centrifugal Pump Using Radial Basis Function Metamodels. *Adv. Mech. Eng.* **2014**, *6*, 457542. [CrossRef]
20. Shigemitsu, T.; Ogawa, Y.; Nakaishi, E. PIV measurement of internal flow in mini centrifugal pump. *IOP Conf. Ser. Earth Environ. Sci.* **2019**, *240*, 032026. [CrossRef]
21. Ni, D.; Lu, H.; Huang, S.; Lu, S.; Zhang, Y. Experimental Study on PIV Measurement and CFD Investigation of the Internal Flow Characteristics in a Reactor Coolant Pump. *Energies* **2023**, *16*, 4345. [CrossRef]
22. Tan, L.; Wang, W.; Shi, W.; Yang, Y.; Bao, L.; Wang, C.; Wang, T.; Li, H. A study on the internal vortex structure within a single-blade pump via numerical methods and particle image velocimetry experiments. *Phys. Fluids* **2024**, *36*, 115130. [CrossRef]
23. Černý, J.; Polák, M. Analysis of Fluid Flow in a Radial Centrifugal Pump. *Processes* **2023**, *11*, 448. [CrossRef]
24. Jiang, L.; Zhao, Y.; Zhao, Z.; Guo, T.; Bai, L.; Zhou, L. CFD-DEM simulation and experimental study of particle dynamics in a solid-liquid two-phase centrifugal pump. *Adv. Powder Technol.* **2025**, *36*, 105077. [CrossRef]
25. Afridi, A.; Al Rashid, A.; Koç, M. Recent advances in the development of stereolithography-based additive manufacturing processes: A review of applications and challenges. *Bioprinting* **2024**, *43*, e00360. [CrossRef]
26. Jahanmir, S.; Hunsberger, A.Z.; Ren, Z.; Heshmat, H.; Heshmat, C.; Tomaszewski, M.J.; Walton, J.F. Design of a small centrifugal blood pump with magnetic bearings. *Artif. Organs* **2009**, *33*, 714–726. [CrossRef]
27. Masuzawa, T.; Kita, T.; Matsuda, K.; Okada, Y. Magnetically suspended rotary blood pump with radial type combined motor-bearing. *Artif. Organs* **2000**, *24*, 468–474. [CrossRef] [PubMed]
28. Wang, C.N.; Yang, F.C.; Nguyen, V.T.T.; Vo, N.T.M. CFD Analysis and Optimum Design for a Centrifugal Pump Using an Effectively Artificial Intelligent Algorithm. *Micromachines* **2022**, *13*, 1208. [CrossRef]
29. Li, H.; Chen, Y.; Yang, Y.; Wang, S.; Bai, L.; Zhou, L. CFD Simulation of Centrifugal Pump with Different Impeller Blade Trailing Edges. *J. Mar. Sci. Eng.* **2023**, *11*, 402. [CrossRef]
30. Li, W. Performance of vortex pump in CFD simulations with rough walls. *Int. J. Fluid Eng.* **2025**, *2*, 013902. [CrossRef]
31. Liu, J.-N.; Wang, D.; Huang, X. Investigation of turbulence models for aerodynamic analysis of a high-pressure-ratio centrifugal compressor. *Phys. Fluids* **2023**, *35*, 106108. [CrossRef]
32. Speziale, C.; Thangam, S. Analysis of an RNG based turbulence model for separated flows. *Int. J. Eng. Sci.* **1992**, *30*, 1379–1388. [CrossRef]
33. Liu, G.; Chan, W.K. Effects of Flow Coefficient on Miniature Centrifugal Pump Performance. *J. Fluids Eng.* **2018**, *141*, 031103. [CrossRef]
34. Li, C.; Qiu, H.; Ma, J.; Wang, Y. Numerical study on the performance of centrifugal blood pump with superhydrophobic surface. *Int. J. Artif. Organs* **2022**, *45*, 1028–1036. [CrossRef]
35. Borisut, P.; Nuchitprasittichai, A. Adaptive Latin Hypercube Sampling for a Surrogate-Based Optimization with Artificial Neural Network. *Processes* **2023**, *11*, 3232. [CrossRef]
36. Wang, W.; Pei, J.; Yuan, S.; Zhang, J.; Yuan, J.; Xu, C. Application of different surrogate models on the optimization of centrifugal pump. *J. Mech. Sci. Technol.* **2016**, *30*, 567–574. [CrossRef]
37. Cao, W.; Wang, H.; Yang, X.; Leng, X. Optimization of Guide Vane Centrifugal Pumps Based on Response Surface Methodology and Study of Internal Flow Characteristics. *J. Mar. Sci. Eng.* **2023**, *11*, 1917. [CrossRef]
38. Sahebi-Kuzeh Kanan, R.; Niroomand-Oscuii, H.A.-O.; Badri Ghavifekr, H.; Ghalichi, F. Design and prototyping of a magnetically and hydrodynamically suspended blood pump via multiobjective optimization. *Sci. Rep.* **2025**, *15*, 26171. [CrossRef]
39. Zhang, Y.; Hu, S.; Wu, J.; Zhang, Y.; Chen, L. Multi-objective optimization of double suction centrifugal pump using Kriging metamodels. *Adv. Eng. Softw.* **2014**, *74*, 16–26. [CrossRef]
40. Lima, J.P.S.; Vieira, R.L.; dos Santos, E.D.; Rocha, L.A.O.; Isoldi, L.A. Multi-Objective Optimization Based on Kriging Surrogate Model and Genetic Algorithm for Stiffened Panel Collapse Assessment. *Appl. Mech.* **2025**, *6*, 34. [CrossRef]
41. Moustapha, M.; Galimshina, A.; Habert, G.; Sudret, B. Multi-objective robust optimization using adaptive surrogate models for problems with mixed continuous-categorical parameters. *Struct. Multidiscip. Optim.* **2022**, *65*, 357. [CrossRef]
42. Zhao, J.; Pei, J.; Yuan, J.; Wang, W. Energy-saving oriented optimization design of the impeller and volute of a multi-stage double-suction centrifugal pump using artificial neural network. *Eng. Appl. Comput. Fluid Mech.* **2022**, *16*, 1974–2001. [CrossRef]
43. Wang, X.D.; Hirsch, C.; Kang, S.; Lacor, C. Multi-objective optimization of turbomachinery using improved NSGA-II and approximation model. *Comput. Methods Appl. Mech. Eng.* **2011**, *200*, 883–895. [CrossRef]
44. Shim, H.-S.; Kim, K.-Y.; Choi, Y.-S. Three-Objective Optimization of a Centrifugal Pump to Reduce Flow Recirculation and Cavitation. *J. Fluids Eng.* **2018**, *140*, 091202. [CrossRef]
45. Dokiparti, S.; Doshi, A.; Bade, M.H. Centrifugal pump performance improvement using back cavity filling. *Phys. Fluids* **2024**, *36*, 067129. [CrossRef]

46. Li, J.; Li, Y.; Lian, J.; Wei, L.; Zhang, R. Experimental study on transient self-priming process of rotary lobe pump. *Flow Meas. Instrum.* **2025**, *102*, 102803. [CrossRef]
47. Wang, J.; Dang, J.; Yang, T.; Zhang, R. Experimental study on hydraulic performance optimization of ultra-low specific speed centrifugal pump. *Phys. Fluids* **2024**, *36*, 082114. [CrossRef]

Disclaimer/Publisher's Note: The statements, opinions and data contained in all publications are solely those of the individual author(s) and contributor(s) and not of MDPI and/or the editor(s). MDPI and/or the editor(s) disclaim responsibility for any injury to people or property resulting from any ideas, methods, instructions or products referred to in the content.